Comparative performance evaluation of candidate receivers for an etendue-conserving compact linear Fresnel mirror field

A.E. Rungasamy, K.J. Craig* and J.P. Meyer

Department of Mechanical and Aeronautical Engineering, University of Pretoria, Pretoria 0002, South Africa.

*Corresponding author: ken.craig@up.ac.za

Abstract

While several studies of multitube and monotube linear Fresnel receivers exist in the literature, comparative studies on different types of receivers are limited. This paper therefore aims to address this gap within literature by comparing the optical and thermal performance of four different receivers: an adapted compound parabolic concentrator (CPC)-type monotube receiver, an adapted tailored edge ray concentrator (TERC)-type monotube receiver, a trapezoidal multitube receiver and an adapted TERC-type multitube receiver. Existing literature was used to determine the design elements limiting heat loss, which were then incorporated into the receiver design and optical optimisation of the four receivers. Once the geometry was determined through a series of Monte Carlo ray tracing (MCRT) simulations, a validated two-dimensional computational fluid dynamic (CFD) model was used to determine the heat loss of each receiver for the same thermal conditions. Given that these heat loss studies were decoupled from the optical study, they are valid for any type of mirror field. While both adapted TERC-type receivers performed well optically (with daily optical efficiencies of 56.93% and 56.6% for the monotube and multitube receivers, respectively), the adapted TERC-type multitube receiver had the highest thermal loss of all the receivers, increasing the heat loss of the TERC-type monotube receiver by a factor of 2.5. In contrast, the adapted CPC-type monotube receiver had a lower daily optical efficiency of 51.29% when paired with an etendue-conserving compact linear Fresnel mirror field, but had low thermal loss, second only to the lower heat loss of the adapted TERC-type monotube receiver by a factor of 1.26. The standard trapezoidal receiver had a relatively low daily optical efficiency of 53.69% and relatively high heat losses, higher than the adapted CPC- and TERC-type monotube receivers by a factor of 1.5 and 1.9, respectively. The adapted TERC-type monotube receiver was therefore determined to be the best candidate receiver for an etendue-conserving compact linear Fresnel field.

Keywords: *Linear Fresnel receiver, thermal losses, Monte Carlo ray tracing, computational fluid dynamics, monotube receiver, multitube receiver, secondary*

Nomenclature

Nomenclature			
$A_{aperture}$	Mirror aperture area	t_b	Insulation thickness on back wall
A_p	Absorber tube area	t_w	Insulation thickness on side walls
b	Width of the inner back wall of the receiver	W_A	Receiver aperture width
C	Receiver secondary gradient	x_{dom}	Size of computational domain in *x*
c	Receiver depth	x_T	Transition point in *x* from single to multitarget mirrors
c_1	Dimensional constant of the overall heat loss coefficient	y_{dom}	Size of computational domain in *y*
Δx	Distance from receiver centre to right boundary	y_T	Transition point in *y* from single to multitarget mirrors
Δy	Distance from receiver centre to bottom boundary	**Greek symbols**	
D	Distance between receivers	α	Absorptance

Nomenclature			
d_1	Exponential constant of the overall heat loss coefficient	β	Interior angle of receiver
		ε	Emissivity
$error$	Computational error	η_{opt}	Optical efficiency
f_x	Secondary focal point in x	ξ	Receiver rotation angle
f_y	Secondary focal point in y	τ	Transmissivity
H	Receiver height	**Abbreviations**	
N_T	Number of absorber tubes	CPC	Compound parabolic concentrator
OD_{tube}	Absorber tube outer diameter	CFD	Computational fluid dynamics
P_i	the number of rays used within the simulation	DNI	Direct normal irradiation
$\bar{P}_i$	norm of the number of rays incident on a surface	DO	Discrete ordinate
p	Distance between absorber tubes	ECCLFR	Etendue conserving compact linear Fresnel reflector
Q_{exp}	Experimental heat loss	LFR	Linear Fresnel reflector
Q_{sim}	Simulation based heat loss	MCRT	Monte Carlo ray tracing
$\dot{Q}_{T,available}$	Energy available to the field	RTE	Radiative transfer equation
$\dot{Q}_{T,absorbed}$	Absorbed energy by the absorber tubes	SMS	Simultaneous multisurface
T_{pipe}	Absorber tube temperature	TERC	Tailored edge ray concentrator
T_∞	Ambient temperature		

1. Introduction

Concentrating solar power generates electricity by utilising solar energy as the heat source in a thermoelectric power cycle. Solar radiation is either reflected or refracted onto a target (the receiver), where a temperature difference is induced within a heat transfer fluid (Kalogirou, 2014; Lovegrove and Stein, 2020). While most of the radiation within the receiver is absorbed, some of the energy is lost through thermal reradiation, conduction and convection (Reynolds et al., 2004). In order to maximise the amount of energy transferred to the fluid, the receiver must be designed on both an optical and a thermal basis; the amount of solar radiation captured must be maximised, while the thermal loss must be minimised (Dey, 2004). This paper addresses this design challenge for a line-focusing plant (linear Fresnel) as these plants undergo a large variety of thermal conditions, depending on the longitudinal location along the collector field. The corollary to this is that line-focusing plants can be easily scaled for the required power or thermal output by changing the length of the plant.

While early linear Fresnel receivers took the form of flat receivers(Goswami et al., 1990b; Mathur et al., 1991a; Mathur et al., 1991b; Singh et al., 1980; Singhal et al., 1982), single tubes (Choudhury and Sehgal, 1986; Mathur et al., 1991a; Mathur et al., 1991b; Negi et al., 1989; Sootha and Negi, 1994) and simple cavities (Dey, 2004; Feuermann and Gordon, 1991; Pye et al., 2003; Reynolds et al., 2004; Singh et al., 1999), most modern receivers make use of a cavity receiver design to reduce spillage.

The two most prominent receiver designs proposed for LFR systems are that of a monotube receiver and a multitube receiver. Extensive literature exists for both designs, but there is little to no direct comparison of these types of receivers within the current literature, making it difficult to determine what receiver design is most appropriate to pair with different linear Fresnel mirror fields. The aim of this paper is therefore to compare multiple receiver designs on an optical and thermal basis in order to determine which design is best to pair with a novel etendue-conserving compact linear Fresnel reflector (ECCLFR) field (Chaves et al., 2017; Chaves and Collares-Pereira, 2010; Rungasamy et al., 2019; Rungasamy, 2020), as shown in Figure 1.

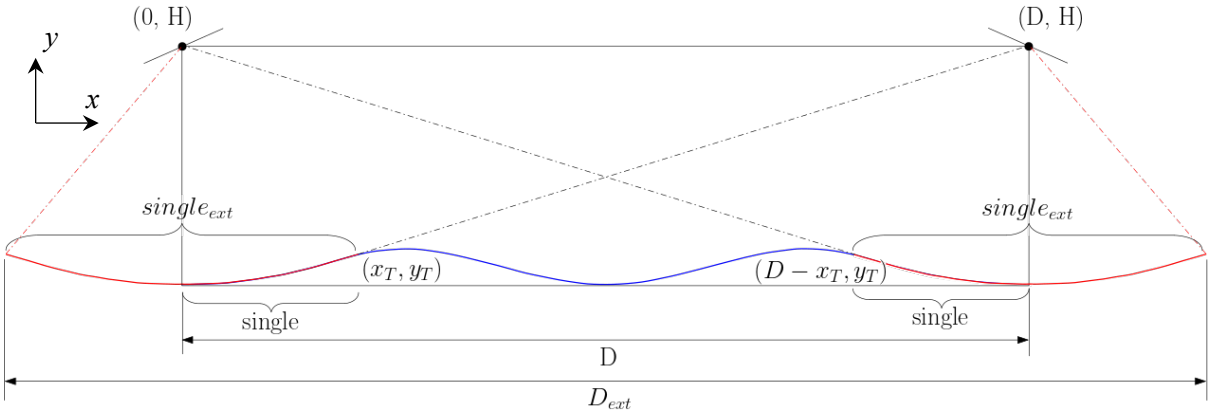

Figure 1 Etendue-conserving compact linear Fresnel field showing two receiver target points

The single target section (indicated in red) exclusively targets the receiver closest to it while the multitarget section (indicated in blue) alternates between the two receiver targets. This type of field significantly enhances the optical efficiency of a standard linear Fresnel mirror field, from η_{opt} = 66% to η_{opt} = 74% for an etendue-conserving compact linear Fresnel field (Guerreiro et al., 2011). Rungasamy et al. (2019) compared different mirror layouts for this type of field and found that the condition of no blocking and shading resulted in the highest daily optical efficiencies. Figure 2 gives an example of this field layout.

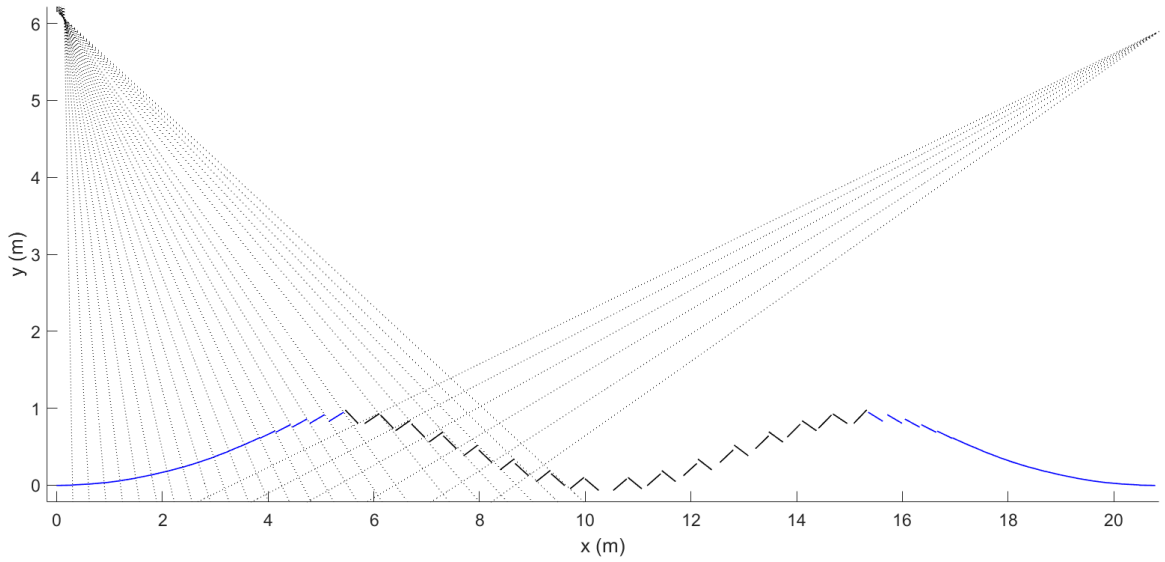

69 **Figure 2** Etendue-conserving compact linear Fresnel field with a condition of no blocking and shading (Rungasamy et al., 2019)

The most promising receiver designs were selected from literature, and these receivers were optically optimised using a series of MCRT simulations to determine their optical performance when evaluated in conjunction with the primary reflector field for daily performance at a zero azimuth angle. The next sections discuss monotube and multitube receivers to review state-of-the-art designs. This is followed by an optimisation section that evaluates the optical performance of combinations of receiver candidates. Where possible, design elements from the literature study identified as measures effective in limiting thermal loss were integrated into the design. The thermal loss of each receiver is then determined using two-dimensional CFD studies. This process aimed to ensure that the best version of each receiver design is used within the comparison so that the result was not unduly influenced by the specific geometric parameters used. It is worth noting that, while the optical performance was dependent on the primary field used in this paper, the thermal studies are valid for any primary field.

2. Monotube receivers

There are many studies pertaining to both the optical and thermal design of monotube-type receivers. The optical design of a monotube receiver consists primarily of determining the shape of the secondary reflector. The word "secondary" refers to any secondary reflecting surface that is used in conjunction with the absorber tube(s). A variety of secondary shapes have been proposed over the years, ranging from simple flat secondaries (Singh et al., 1999) to a simultaneous multisurface (SMS)-based design (Guerreiro et al., 2015). The optical efficiencies associated with each mirror field and secondary design, as obtained from literature, are listed in Table 1. This efficiency (η_{opt}) is defined as the ratio is between the available energy ($\dot{Q}_{T,available}$) on the aperture of the mirror field and the energy absorbed by the absorber tubes ($\dot{Q}_{T,absorbed}$).

$$\eta_{opt} = \frac{\dot{Q}_{T,absorbed}}{\dot{Q}_{T,available}} \quad (1)$$

As the absorbed radiation is affected by the mirror reflectivity (ρ), the glass transmissivity (τ) and the absorber absorptivity (α), these properties are also listed in Table 1.

Table 1 Optical efficiency of different secondaries for monotube receivers

Secondary type	Optical efficiency η_{opt} (%)	Emissive properties	References
None	37	ρ = 0.65, α = 0.91	(Khan and Khamrul, 1999)
Flat	50.6; 70.9 with optimised targeting	ρ = 0.94, τ = 0.96, α = 0.92	(Chaitanya Prasad et al., 2017)
	63	ρ = 0.94, τ = 0.97, α = 0.96	(Hack et al., 2017)
Parabolic	61	ρ = 0.94, τ = 0.95, α = 0.92	(Bellos et al., 2018a)
Segmented parabolic	67; 76.4 with optimised targeting	ρ = 0.94, τ = 0.96, α = 0.92	(Chaitanya Prasad et al., 2017)
Compound parabolic concentrator (CPC)	76.1; 74.9 with optimised targeting	ρ = 0.94, τ = 0.96, α = 0.92	(Chaitanya Prasad et al., 2017)(Hack et al., 2017)
	70	ρ = 0.94, τ = 0.97, α = 0.96	
	65	ρ = 0.95, τ = 0.95, α = 0.96	(Qiu et al., 2015)
Butterfly/gull-wing	42	ρ = 0.94, τ = 0.97, α = 0.96	(Hack et al., 2017)
	78	ρ = 0.94, τ = 0.95, α = 0.95	(Grena and Tarquini, 2011)
Simultaneous multisurface (SMS)	74	ρ = 0.92, τ = 0.96, α = 0.95	(Canavarro et al., 2014)
Tailored edge ray concentrator (TERC)	77.2	ρ = 0.935, τ = 0.965, α = 0.955	(Horta et al., 2011)
Compound elliptical concentrator	70	ρ = 0.94, τ = 0.97, α = 0.96	(Canavarro et al., 2016)
Adaptive	69.9	ρ = 0.94, τ = 0.97, α = 0.96	(Zhu, 2017)
	72		(Hack et al., 2017)
Adaptive optimisation	78	ρ = 0.93, τ = 0.93, α = 1	(Vouros et al., 2019)
Bezier polynomial	72.8	ρ = 0.94, τ = 0.95, α = 0.92	(Bellos et al., 2018b)

The CPC type secondary remains one of the best-performing secondaries available, outperforming all other conventional shapes and performing similarly to the optimised secondaries proposed. Therefore, it establishes a good basis of comparison for the performance of any receiver. While both the adaptive secondary and the Bezier polynomial secondary performed well, the resultant shape is relatively similar to the CPC type secondary. Of the novel secondary shapes (SMS, TERC and CPC), the TERC performed the best. The CPC and TERC type secondary shapes were therefore chosen for the receiver comparison in the next sections.

On a thermal design basis, a glass layer is typically used to reduce convection and radiation thermal losses in the monotube receiver. It is included at the front of the receiver cavity or concentrically around the absorber tube with either air (encapsulated design) or a vacuum (evacuated design) in the annulus. Figure 3(a) illustrates the heat loss mechanisms for the cover design, while Figure 3(b) illustrates the heat loss mechanisms for an encapsulated design. The heat loss mechanisms for the evacuated design are the same as for the encapsulated design, except that little to no convective losses occur within the annulus in the latter.

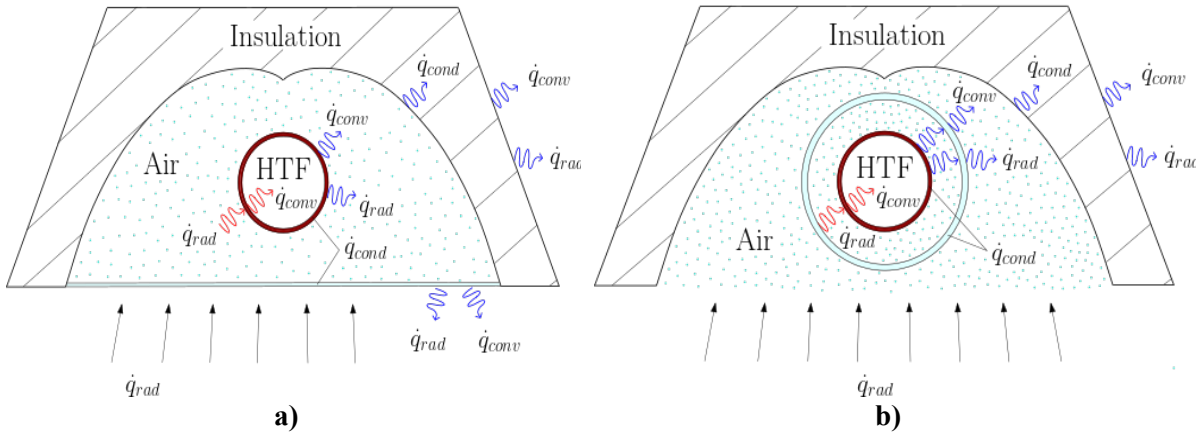

Figure 3a) Glass cover; and **b)** encapsulated monotube receiver design

In all studies comparing the three configurations, the evacuated design had the lowest heat loss by a significant margin; however, there were mixed results in the comparison between the envelope and cover designs (Cagnoli et al., 2018; Hofer et al., 2015; Montes et al., 2017a; Montes et al., 2017b). Reddy et al. (2018) report a heat loss reduction of approximately 65 to 70% due to evacuation of the annulus. Given the dramatic reduction of heat loss within an evacuated design, the monotube receivers used within the comparison made use of this thermal design element. Evacuating a linear-focus receiver has obvious cost implications that need to be considered in a holistic evaluation, but this was not performed here. Cognisance is, however, taken of the fact that parabolic trough designs mostly include this element.

3. Multitube receivers

The field of multitube receiver research focuses almost exclusively on thermal design. Although early multitube receiver designs consisted of different cavity shapes, research has largely converged towards a trapezoidal cavity shape, as this shape allows for a larger acceptance angle (Pye, 2008) and better insulation of the hottest parts of the receiver. Figure 4 shows the layout of a typical trapezoidal multitube receiver. Due to variation in the diameter and number of tubes, a glass cover is typically used at the front of the cavity and the cavity is filled with air. The heat transfer mechanisms operate in a similar way to the monotube receiver with a glass cover; with the addition of each tube interacting thermally with one another, creating a degree of interdependence between the different heat transfer mechanisms (Reynolds et al., 2004).

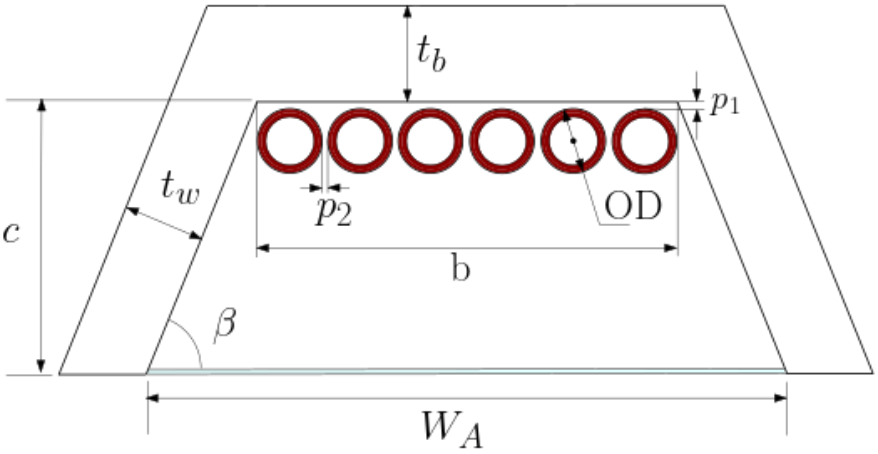

Figure 4 Multitube receiver geometry and definition of parameters

The geometry and thermal interactions within a multitube receiver are complex (Jance et al., 2003), making modelling each heat loss analytically challenging. Therefore, many studies use finite volume models/CFD or experimental results to derive correlations for a simplified analytical model. The most common correlation used is an overall heat loss coefficient (Singh et al., 2010a), defined based on the overall heat loss (Q_{loss}), absorber tube area (A_p) and difference between the tube temperature (T_{pipe}) and the ambient temperature (T_∞) as follows:

$$U_L = \frac{Q_{loss}}{A_p(T_{pipe} - T_\infty)} \quad (2)$$

This dimensional coefficient forms a power curve when expressed in terms of absorber temperatures (Khan and Khamrul, 1999; Negi et al., 1989; Singh et al., 2010a). Therefore, the overall heat loss coefficient is expressed as follows:

$$U_L = c_1 \cdot (T_{tube})^{d_1} \text{ or } U_L = c_1 \cdot (T_{tube} - T_\infty)^{d_1} \quad (3)$$

with c_1 a dimensional constant with the temperature unit depending on the value of d_1. The use of this coefficient both in and across different studies allows the interpretation of the effect of different design parameters for a multitube receiver design. Table 2 lists the overall heat loss coefficient expressions derived from different receiver heat loss studies in the literature and the associated applicable temperature ranges. The parameters used are defined in Figure 4.

Table 2 Overall heat loss coefficient for different multitube receiver thermal studies

	Tube temperature T_{tube} (°C)	**Correlation for overall heat loss coefficient (W/m²K)**	**Receiver specifications**
Singh *et al.*, 2010a; 2010b	75–175		W_A = 400 mm; c = 100 mm; β = 34°; variable t_w t_b = 125 mm; glass wool
		$U_{L1} = 0.3521 \cdot T_{tube}^{0.6076}$	Rectangular tube; b = 100 mm; black paint ε_{tube} = 0.17; single glass
		$U_{L2} = 0.461 \cdot T_{tube}^{0.513}$	Double glass
		$U_{L3} = 0.2687 \cdot T_{tube}^{0.5858}$	Rectangular tube; b = 100 mm; selective coating; ε_{tube} = 0.9; single glass

	Tube temperature T_{tube} (°C)	Correlation for overall heat loss coefficient (W/m²K)	Receiver specifications
		$U_{L4} = 0.2507 \cdot T_{tube}^{0.5843}$	Double glass
		$U_{L5} = 0.5805 \cdot T_{tube}^{0.4903}$	Six round tubes with OD_{tube} = 16 mm; black paint; ε_{tube} = 0.17; single glass
		$U_{L6} = 0.56 \cdot T_{tube}^{0.4661}$	Double glass
		$U_{L7} = 0.5637 \cdot T_{tube}^{0.4456}$	Six round pipes with OD_{tube} = 16 mm; selective coating; ε_{tube} = 0.9; single glass
		$U_{L8} = 0.3848 \cdot T_{tube}^{0.4973}$	Double glass
Facão and Oliveira, 2011	110–230	$U_{L9} = 0.0309 \cdot (T_{tube} - T_{\infty})^{0.389}$	W_A = 124 mm; c = 45 mm; β = 50°; t_w = 35 mm; t_b = 35 mm; rock wool; N_T = 6; OD_{tube} = 15.875 mm; ε_{tube} = 0.49
Flores Larsen et al., 2012	110–285	$U_{L10} = 0.357 \cdot (T_{tube} - T_{\infty})^{0.5184}$	W_A = 685 mm; c = 220 mm; β = 45°; t_w = 120 mm; t_b = 120 mm; rock wool; N_T = 5; OD_{tube} = 33 mm; ε_{tube} = 0.88
Manikumar and Valan Arasu, 2014	95–140		w_A = 196 mm; c = 45 mm; β = 50°; variable t_w; t_b = 35 mm; glass wool
		$U_{L11} = 0.53 \cdot T_{tube}^{0.52}$	Plate b = 120 mm; no coating; ε_{plate} = 0.87
		$U_{L12} = 0.14 \cdot T_{tube}^{0.74}$	Plate b = 120 mm; coating; ε_{plate} = 0.17
		$U_{L13} = 0.37 \cdot T_{tube}^{0.62}$	Six round tubes with OD_{tube} = 15.8 mm; no coating; ε_{tube} = 0.87
		$U_{L14} = 0.37 \cdot T_{tube}^{0.58}$	Six round tubes with OD_{tube} = 15.8 mm; coating; ε_{tube} = 0.17
Moghimi et al., 2015	76.85–226.85	$U_{L15} = 0.3341 \cdot (T_{tube} - T_{\infty})^{0.4443}$	W_A = 1231.3 mm; c = 240 mm; β = 30°; t_w = 40 mm; t_b = 85 mm; glass wool; N_T = 4; OD_{tube} = 50 mm; p = 75 mm; ε_{tube} = 0.95

Figure 5 plots the overall heat loss coefficients of Table 2 for the temperature range specified in these studies.

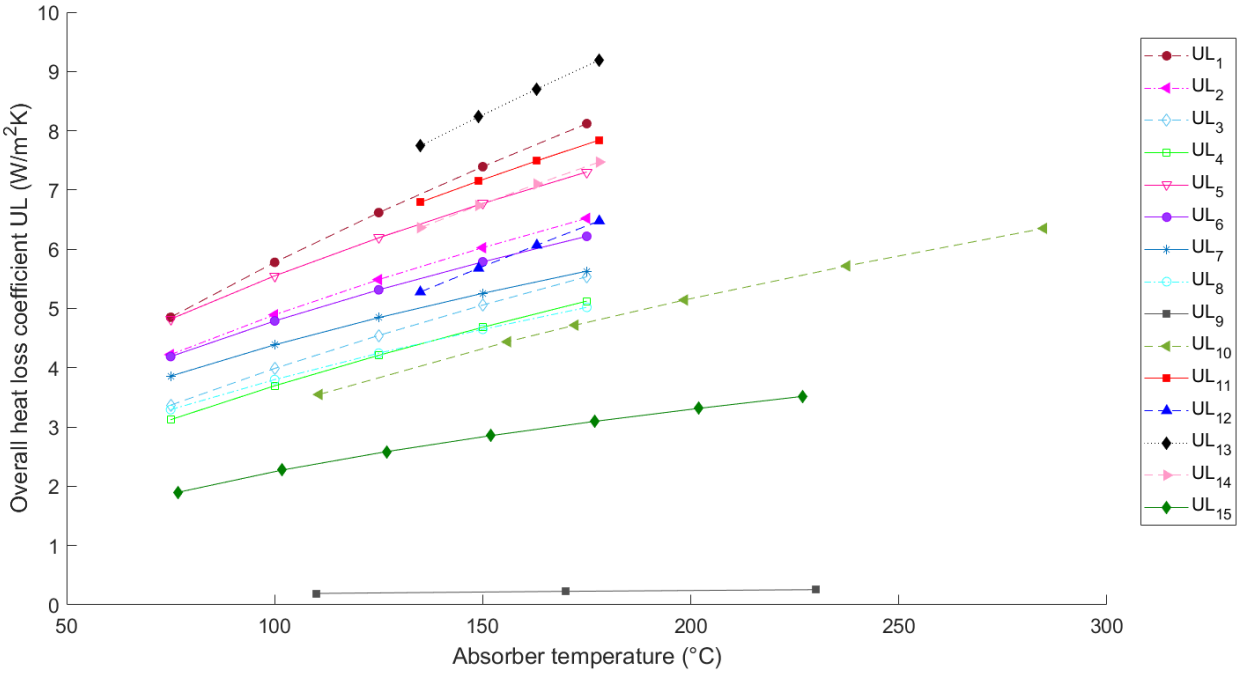

Figure 5 Overall heat loss coefficients for different multitube receiver thermal studies

The following trends were found:

- The use of a selective coating rather than black paint reduces heat losses within the receiver. Singh et al. (2010b) and Sahoo et al. (2013b) each reported a 20 to 30% reduction in heat loss, while Manikumar and Valan Arasu (2014) reported a 16% reduction. Flores Larsen et al. (2012) reported a significantly higher reduction of 37 to 47%. This is due to the fact that selective coatings specifically reduce radiative losses, which have been found to dominate heat loss, especially at higher absorber temperatures (Dey, 2004; Facão and Oliveira, 2011; Flores Larsen et al., 2012; Moghimi et al., 2015; Pye, 2008). This is because radiative losses do not scale linearly with a temperature difference, but rather by the fourth order.
- The heat transfer rate of a round tube is greater than that of a rectangular tube. Pye (2008) reported a 25% increase in heat transfer if the absorber was modelled as multiple tubes rather than assuming a flat surface. This performance difference is due to the larger surface area of multiple pipes rather than a flat surface. However, Manikumar and Valan Arasu (2014) also reported higher overall loss coefficients for the receiver without an absorber plate in front of the tubes. Therefore, while the heat transfer to the fluid increases, the heat loss also increases, and thus the thermal efficiency needs to be assessed rather than the heat transfer. Singh et al. (2010b) reported a 2 to 8% increase in the thermal efficiency of a round tube rather than a rectangular channel, suggesting that the overall effect of using a round tube rather than a flat surface is an increase in performance.

In addition to the above, several studies have investigated the effects of varying parameters within a multitube receiver and reported the following:

- Heat loss increases with an increase in aperture width and receiver depth due to an increase in the surface area of the receiver (Pye, 2008; Pye et al., 2003; Reddy and Kumar, 2014). The sizing of the aperture is particularly important, because up to 91% of total heat loss occurs at the front of the cavity (Flores Larsen et al., 2012; Natarajan et al., 2012). Some studies (Natarajan et al., 2012; Reddy and Kumar, 2014; Saxena et al., 2016) used the aspect ratio $\left(\frac{W}{c}\right)$ between the wall of absorber tubes (W) and the cavity depth (c) in order to non-dimensionalise the effect of the cavity scaling on the heat flux. The resultant expressions for the combined radiation and convection Nusselt number all give a negative exponential correlation (Natarajan et al., 2012; Pye et al., 2003; Saxena et al., 2016). Figure 6 shows the same trend in total heat loss if all other variables are kept constant (Natarajan et al., 2012). Therefore, a shallow cavity with a large wall of absorber tubes

will minimise the heat loss per square metre.

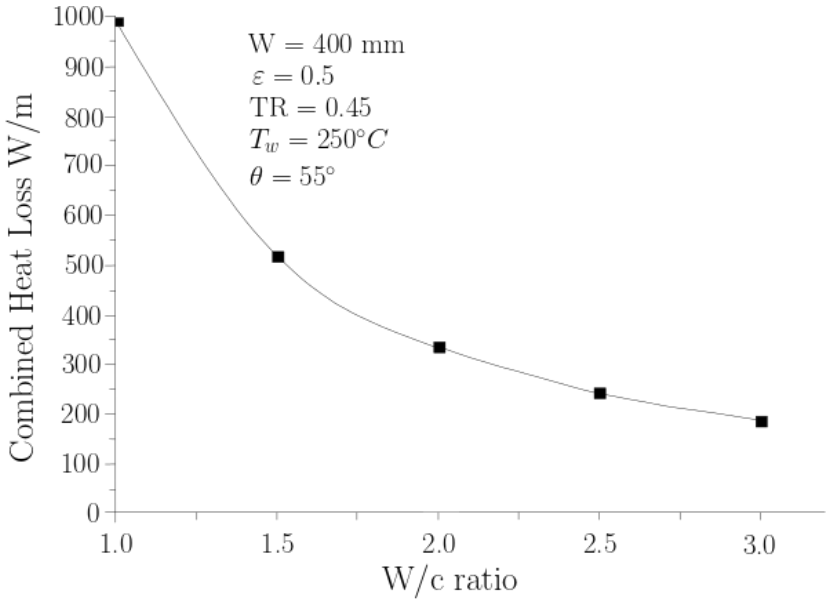

Figure 6 Effect of the aspect ratio between the wall of absorber tubes and cavity depth on the combined heat loss per metre (Natarajan et al., 2012)

- The second cavity parameter of influence is the interior angle of the receiver. While most studies (Dabiri et al., 2018; Moghimi et al., 2015; Natarajan et al., 2012) found that a large interior angle reduced heat flux losses, Saxena et al. (2016) found the opposite to be true. The discrepancy in results is likely due to the non-trivial assignment of independent and dependent variables; Moghimi et al. (2015) and Natarajan et al. (2012) both allowed the aperture width to vary based on the interior angle and cavity depth, while Saxena et al. (2016) allowed the cavity depth to vary. In the latter case, the reduction in interior angle thus also corresponded to a larger aspect ratio $\left(\frac{W}{c}\right)$. Dabiri et al. (2018) allowed the width of the back wall (and therefore, the number of tubes) to vary, but normalised the resultant heat transfer rate by dividing it by the total tube wall length.

- The final cavity parameter of influence is the thickness of the insulation around the cavity. While increasing the thickness of the insulation on the outside of the receiver reduces heat loss, this reduction must be compared with the increase in shadowing on the collector field (Facão and Oliveira, 2011) and with the cost of the insulating material (Moghimi, 2017; Moghimi et al., 2017). Most designs feature thicker insulation at the back of the receiver than around the sides (Manikumar and Valan Arasu, 2014; Moghimi et al., 2015; Singh et al., 2010a; 2010b) because the hottest parts of the receiver are the tubes and the back wall.

- In addition to the cavity itself, the positioning and sizing of the tubes in the receiver are important in multitube receiver design. Tubes should be placed close together and at the back of the cavity to restrict natural convection loss and create the conditions for thermal stratification to take place (Moghimi et al., 2015). In addition, smaller distances between tubes reduce the temperature differences between them (Dey, 2004). Some designs even propose partially embedding the tubes in insulation at the back of the cavity to ensure that heat is only lost through conduction from the top half of the tubes, reasoning that most of the incoming radiation hits the bottom of the tubes (Horta et al., 2011; Reynolds et al., 2004). Lastly, while Abbas et al. (2012) found that reducing the tube diameter increased thermal efficiency, it also increased the pumping power requirements. Therefore, the maximum exergetic efficiency exists in a trade-off region for tube diameters of 0.8 to 3 cm. Dabiri et al. (2018) investigated the effect of varying the tube diameter and number of tubes without considering the pumping power requirements, and the results did not display any clear trends.

In order to incorporate these findings into the subsequent performance comparison, round tubes are placed at the back of the receiver cavity with little space between them. Moreover, if multiple receivers

offer similar optical performance, the receiver with the smaller aperture and shallower cavity should be selected for the thermal study.

Sections 2 and 3 demonstrate the depth of research within the individual design tracks, the results of which will be used for the comparison of different candidate receivers.

4. Thermal modelling assumptions and settings

In order to perform a thermal heat loss study, a variety of assumptions and model settings need to be evaluated to determine their validity and applicability to this model. The first assumption made is that of steady-state heat transfer. While heat losses from an LFR may produce some unsteady flow patterns due to natural and forced convection, Pye (2008) and Moghimi (2017), among others, determined that these transient behaviours had a negligible effect on overall heat loss.

The second assumption made is that a 2D model is sufficient to give a fairly accurate estimation of the heat loss per metre for the receiver. This means that the end loss of the receiver is neglected in the model and that the domain will not include the heat transfer fluid, but rather start on the outer surface of the absorber tube. The chosen boundary condition for the absorber tube surface is a fixed temperature boundary condition, used extensively within thermal literature (Manikumar and Valan Arasu, 2014; Natarajan et al., 2012; Reddy and Kumar, 2014).

While Moghimi (2017), Qiu et al. (2015) and Tsekouras et al. (2018) found that the heat flux distribution correlated strongly with the temperature distribution on the pipe surface, Chang et al. (2014) and Jianfeng et al. (2010) found that the average heat transfer coefficients could be used without introducing significant error. This suggests that, while the circumferential temperature of the absorber tube may vary according to the profile of the incident radiation, this assumption does not necessarily have a significant effect on the total heat loss of the receiver.

While many studies argue that the glass layer in the receiver represents a negligible thermal mass (Dabiri et al., 2018; Flores Larsen et al., 2012; Pye, 2008), this assumption will not be used in this study. This is due to the fact that a portion of the radiation is absorbed by the glass (Moghimi, 2017), causing an increase in temperature and a reduction in heat loss (Heimsath et al., 2014; Sahoo et al., 2013b). Given the significance of radiation in the overall heat loss of the receiver, this effect is likely to be non-negligible and is therefore incorporated into the thermal model.

In order to model spectrally dependent absorption within the glass layer, the discrete ordinates (DO) radiation model is used (Craig et al., 2016), with the banded emissivity properties used listed in Table 13 in the Appendix. The DO radiation model is applicable to a wide range of optical thicknesses, non-grey radiation and semi-transparent walls (ANSYS Inc, 2019a). It solves for the radiative transfer equation (RTE) for a finite number of solid angles specified in the phi and theta directions, with phi being the azimuth angle as defined in the *x*-*y* plane (Figure 1).

For a 2D case, it is sufficient to only increase the control angle count in the phi direction (Craig et al., 2016; Moghimi et al., 2016), while using three discretisations in the polar angle, theta. Within this study, the root mean square surface roughness height of the receiver tubes is much larger than the incident radiation wavelength, resulting in diffuse reradiation from the tube surface (Bennett and Porteus, 1961). A relatively coarse phi discretisation can therefore also be used.

In order to accurately model external natural convection, a section of the surrounding air was included within the CFD domain of each receiver model rather than assuming a convective coefficient. The size of the domain was determined on a case-by-case basis using domain-independent studies. The outer walls of the receiver and cover were modelled in the same way as the inner walls, using a coupled boundary condition with prescribed emissivity values. The outer boundaries of the domain were pressure outlets with a backflow temperature of 300 K and an emissivity of $\varepsilon = 1$.

To model the buoyancy-driven flow associated with natural convection, the body force-weighted pressure solver was used in conjunction with gravity being enabled. The pressure and velocity solvers

were coupled, and pseudo-transient relaxation was activated to obtain a faster convergence rate. While many studies make use of the Boussinesq approximation (Dabiri et al., 2018; Facão and Oliveira, 2011; Pye, 2008; Sahoo et al., 2013a) to model density changes, this assumption is only valid for small changes in temperature; for the large temperature differences typically experienced in a solar receiver, it is likely to yield inaccurate results (Natarajan et al., 2012). Therefore, in this study, the incompressible ideal gas assumption is used to model density changes (Chang et al., 2013; Manikumar and Valan Arasu, 2014; Moghimi, 2017; Tsekouras et al., 2018).

In order to validate these assumptions and model settings, two validation cases were used: an evacuated monotube experimental study (Burkholder and Kutscher, 2009) and a multitube receiver experimental study (Flores Larsen et al., 2012).

5. Validation studies

5.1. Test case I: Evacuated monotube receiver

The evacuated monotube receiver experimental model used by Burkholder and Kutscher (2009) consisted of a Schott 2008 model PTR70 receiver. Although this set-up does not incorporate a receiver secondary, it can be used to validate the settings for the vacuum within the annulus. The absorber tube is made of stainless steel, with a temperature-dependent emissivity, listed in Table 13. The receiver geometry and CFD domain are shown in Figure 7.

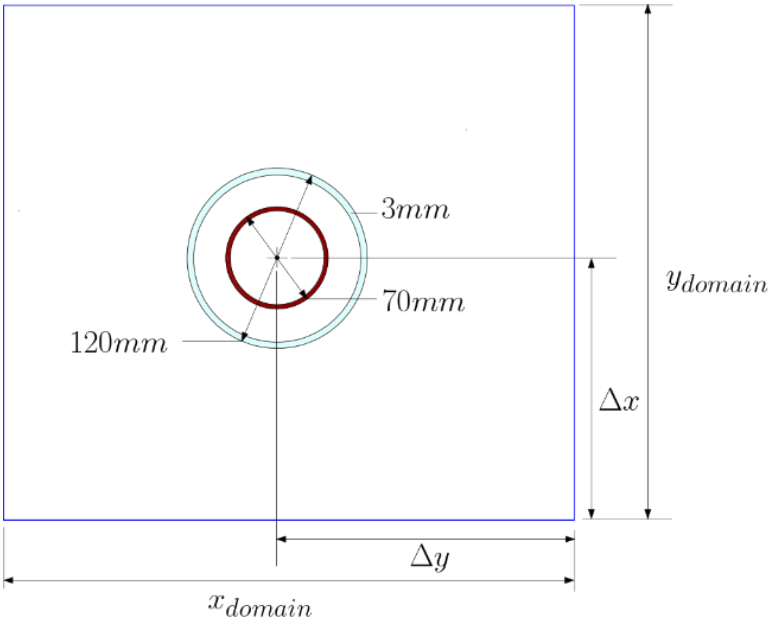

Figure 7 CFD domain for validation test case I

Domain and mesh independence studies were completed, with the error for the studies defined as follows:

$$error_{val} = 100\left(\frac{Q_{sim} - Q_{exp}}{Q_{exp}}\right) \quad (4)$$

A sample mesh and domain is included in Figure 8. In all cases, at least two cells must be present throughout the thin glass layer and the refinement must be sufficient to capture the curvature of the absorber tube.

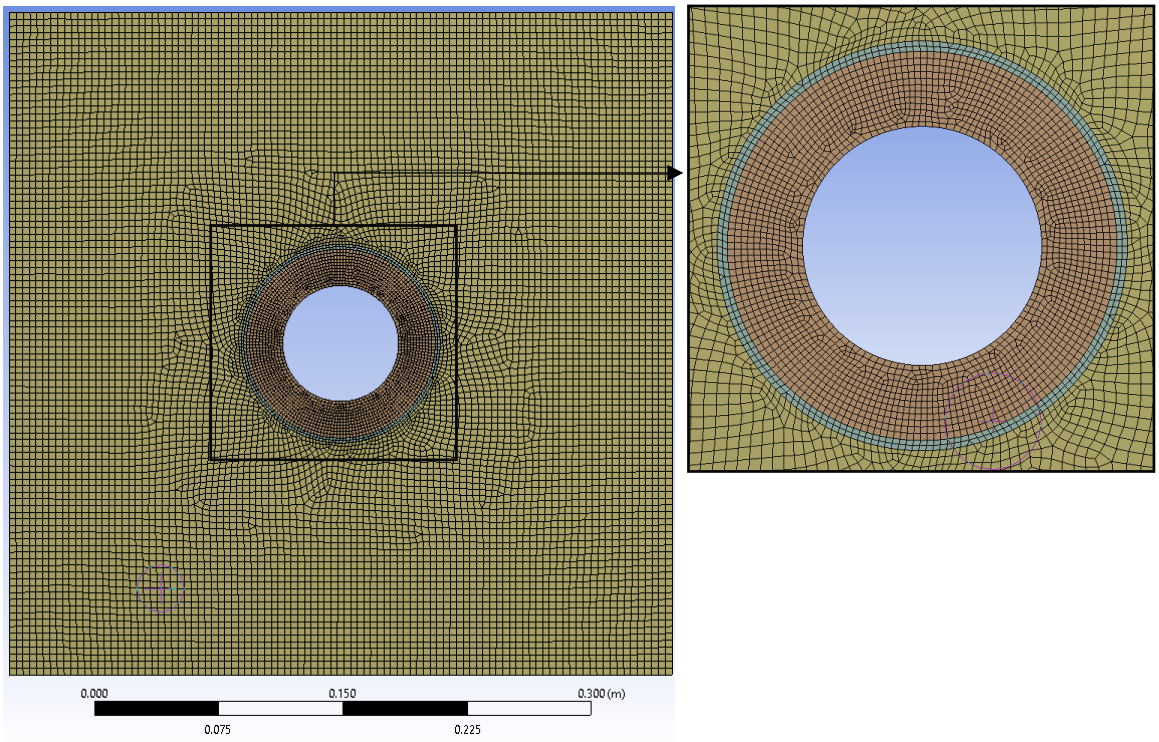

Figure 8 Sample mesh (with close up) and domain size for validation test case I

In the domain independence study, the optimal placement of the receiver was found to be along the vertical axis of symmetry (Δx = 0.5 × domain), due to the symmetric nature of the heat loss. The heat loss result was largely insensitive to changes in the y-position and size of the domain, with all errors less than 1%. Therefore, a small domain of 0.15 m by 0.15 m was used to calculate the heat loss per metre. Figure 9 shows the errors associated with different mesh cell counts in the mesh independence study. While the errors for even very coarse meshes were less than 2%, refinement shows a clear trend in reduction of the error. A fine mesh could be used without disproportionately increasing the computational time because the domain is small. The final mesh used in this test case consisted of 488 707 mixed cells, with a specified face sizing of 0.0001 m for all areas.

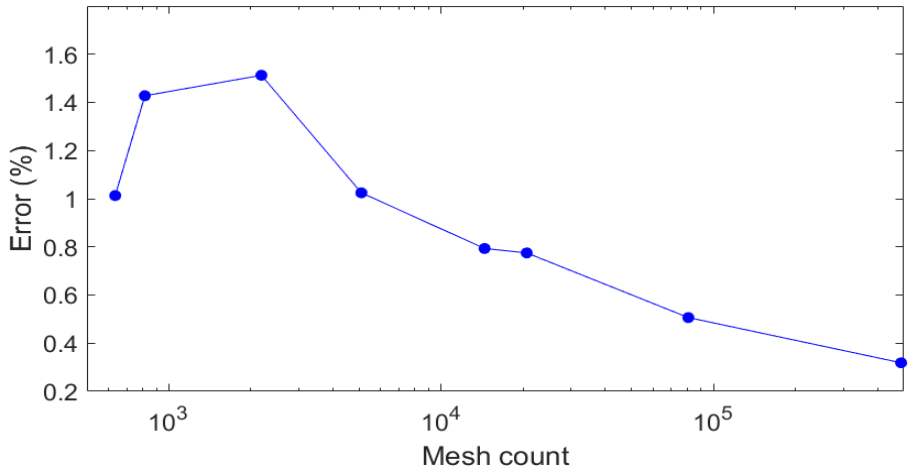

Figure 9 Mesh independence study for validation test case I

The resultant heat losses are listed in Table 3. The CFD model had a maximum error of 3.23% for the lowest tube temperature, with errors less than 1% for most of the temperature ranges considered. The low error values are likely due to the accurately measured emissivity values because radiation dominates the heat loss profile in evacuated monotube receivers.

Table 3 CFD and experimental heat loss per metre for validation test case I

Tube temperature		Emissivity	Heat loss per metre (W/m)		Error (%)
(°C)	(K)		Experimental	CFD	
100	373.15	0.106	15	14.51	-3.23
153	426.15	0.077	23	23.42	1.82
213	486.15	0.074	43	43.15	0.35
246	519.15	0.075	59	59.03	0.05
317	590.15	0.083	113	114.11	0.98
346	619.15	0.084	141	141.59	0.41
390	663.15	0.091	204	204.13	0.06
418	691.15	0.097	257	257.87	0.34
454	727.15	0.103	333	337.03	1.21
458	731.15	0.105	349	351.15	0.62
506	779.15	0.115	495	496.58	0.32

Figure 10 shows the heat loss per metre versus the tube temperature for the experimental and CFD models, as well as a fourth-degree polynomial fit through the data. The 2D CFD model adhered very closely to the experimental graph for the full range of temperatures tested. The fourth-order polynomial also adhered closely to the experimental results, further demonstrating the dominance of radiative losses, as they are driven by a fourth-order temperature difference.

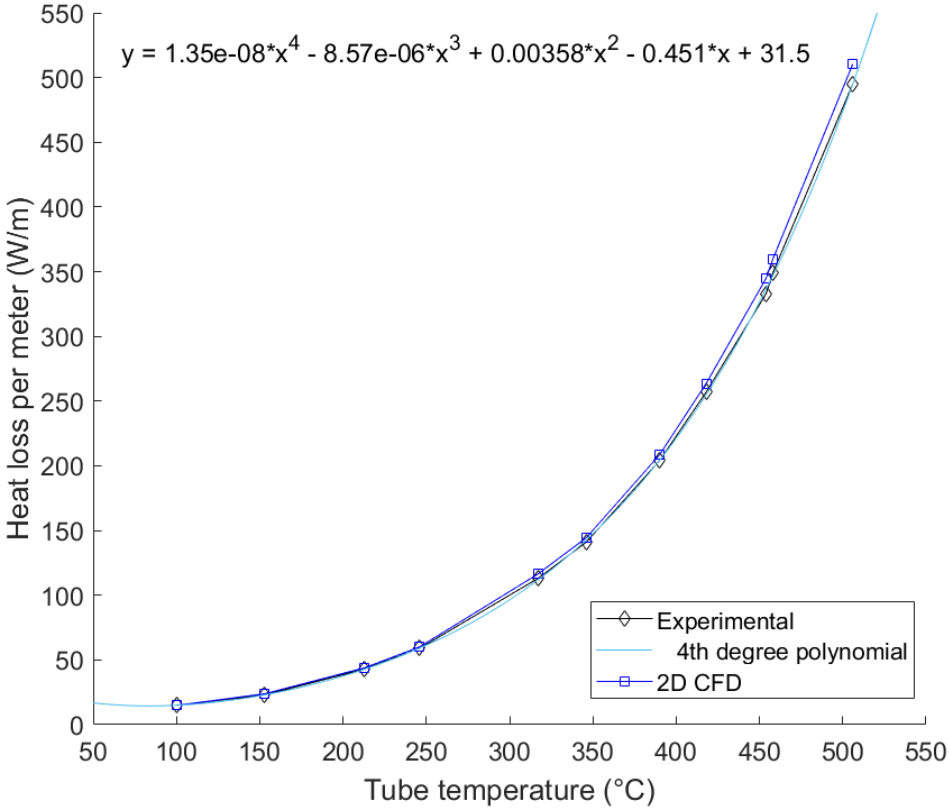

Figure 10 CFD and experimental heat loss per metre for validation test case I

Figure 11 shows the temperature and velocity contours of the receiver for an absorber temperature of 779.15 K (506 °C). The vacuum in the annulus significantly limits the heat loss from the absorber tube, with the temperature on the inside of the glass remaining below 400 K. The plume of hot air rising adheres closely to the surface of the glass envelope due to the Coandă effect, which states that a moving fluid has a tendency to remain attached to an adjacent convex surface (White, 2011).

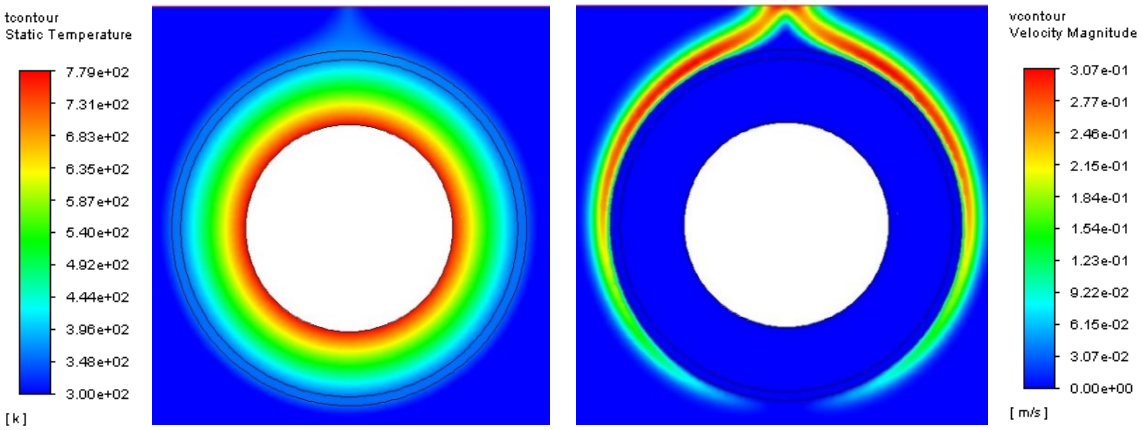

Figure 11a) Thermal; and **b)** velocity magnitude contours for validation test case I

The CFD results obtained from validation test case I are therefore considered to be in good agreement with the experimental results and the expected thermal behaviour based on theory.

5.2 Test case II: Trapezoidal multitube receiver

The experimental model used by Flores Larsen et al. (2012) consisted of five steel tubes with an emissivity of $\varepsilon = 0.88$. The cover of the receiver was made of Mylar film with an emissivity of $\varepsilon = 0.88$, while the outer surface of the cavity of the rock wool insulation was covered in galvanised sheet metal, and the inner surface comprised a polished aluminium sheet with an emissivity of $\varepsilon = 0.1$. The receiver layout and CFD domain are shown in Figure 12, while the material properties used are listed in Table 13.

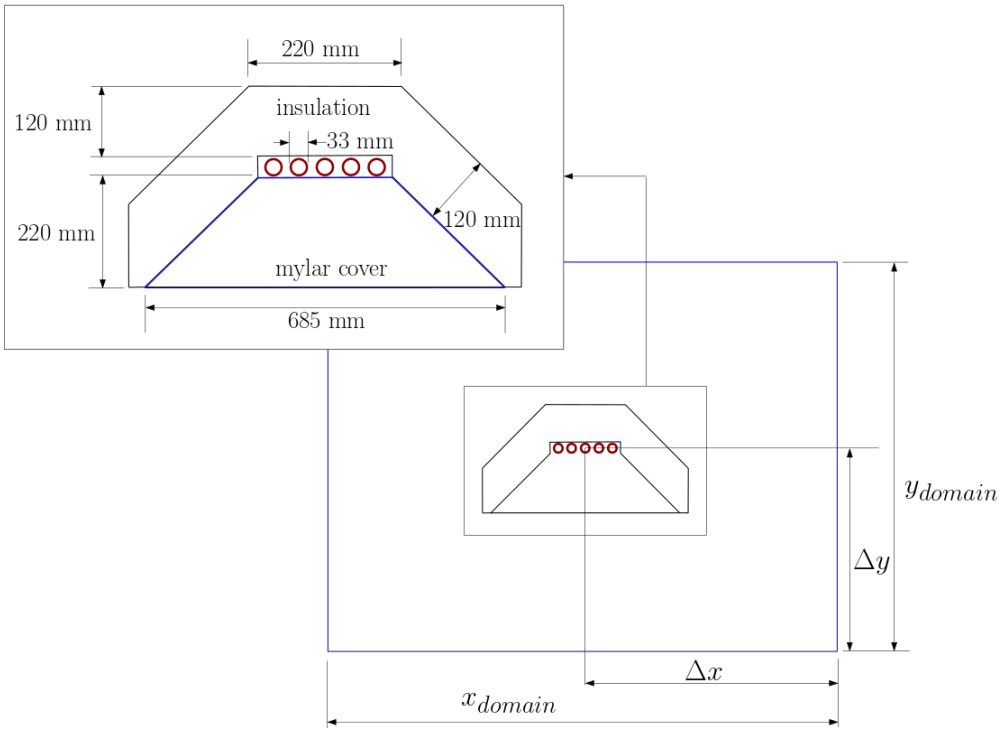

Figure 12 CFD domain for validation test case II

In contrast to validation test case I, the solution was found to be largely dependent on the placement of the pressure outlet boundaries relative to the receiver. Figure 13 shows the error associated with

different domain sizes. It is only for a domain size of 6.5 m by 6.5 m that the error dropped below 2% with a relatively stable thermal plume. For smaller domain sizes, the thermal plume changed direction frequently, creating a dispersive error within the solution.

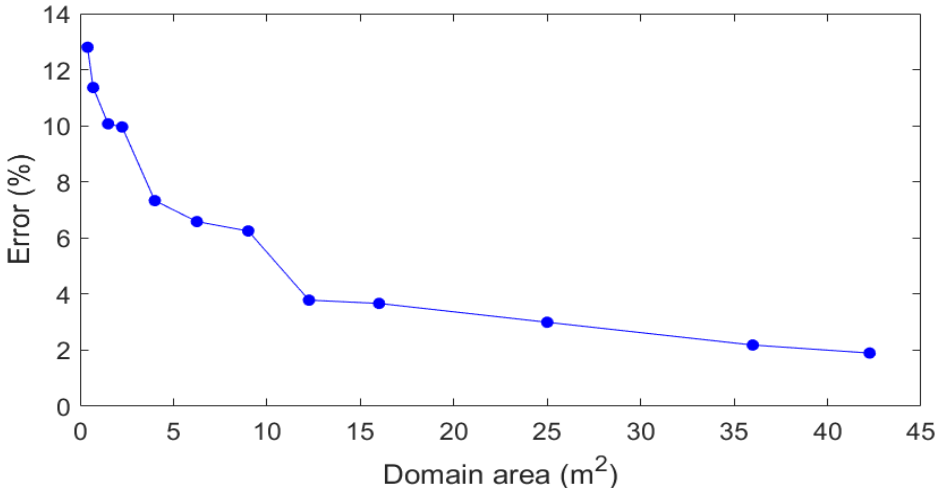

Figure 13 Domain independence study for validation test case II

This solution appears more sensitive to the domain area than to mesh refinement; for mesh cell counts of over 120 000, the solution changed less than 0.2%. The final mesh used consisted of 682 000 cells with a face sizing of 2.5 mm on the receiver cavity, 5 mm on the insulation layer and 8 mm within the domain. Table 4 lists both the experimental (Exp) and simulation-based (Energy plus) heat loss from Flores Larsen et al. (2012), as well as the 2D CFD model heat loss. The largest errors are associated with temperatures below 172.2 °C, with the maximum error of 3.35% associated with the lowest absorber tube temperature (110.7 °C). At lower tube temperatures, convection plays a larger role in the heat losses. Therefore, the instability associated with it becomes more impactful to the overall heat loss assessment. The errors associated with all the other temperatures were all under 2%, with an average error of 1.69%.

Table 4 CFD, simulation and experimental heat loss for validation test case II

Tube temperature (°C)	Ambient temperature (°C)	Heat loss (W)			Error (%)
		Exp	Energy plus	2D CFD	
110.7	37.8	180	201	186.04	3.35
156	25.6	360	398	366.78	1.88
172.2	29.7	430	462	437.35	1.71
198.5	27.6	580	600	574.63	-0.92
237.5	30.3	825	832	809.97	-1.83
284.8	40.2	1130	1166	1135.09	0.45

Figure 14 shows these heat losses versus tube temperature. The 2D CFD model is a better approximation of the experimental results than the simulation results from Flores Larsen et al. (2012), which overpredict heat loss by an average error of 6.18% with a maximum error of 11.84% at a tube temperature of 110.7 °C. The best curve fit of the experimental data is cubic, suggesting that convective and conductive losses affect total heat loss more than in the evacuated monotube model.

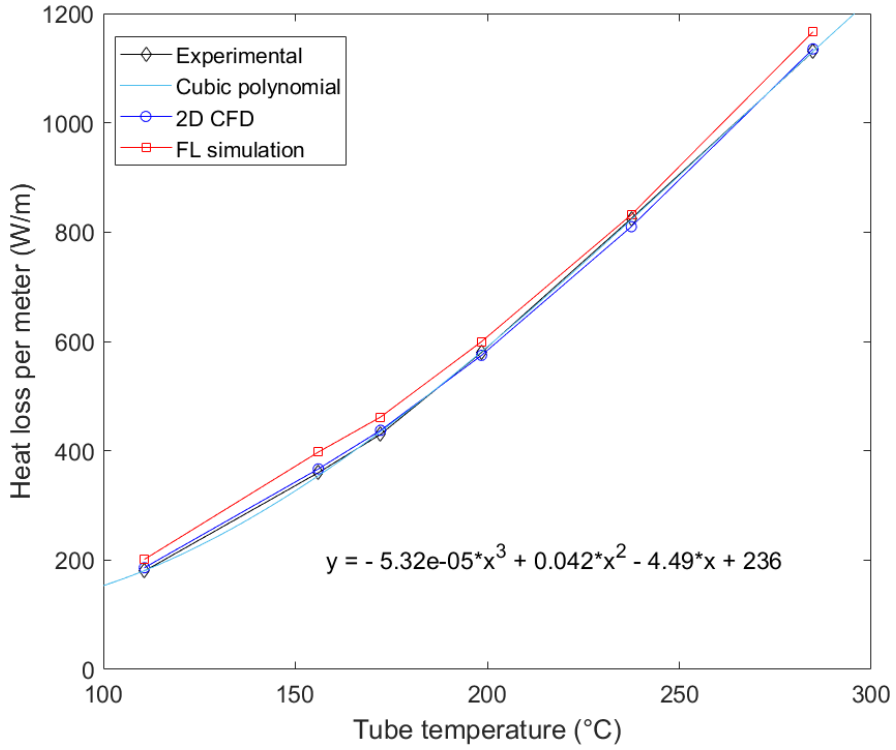

Figure 14 CFD, simulation and experimental heat loss for validation test case II

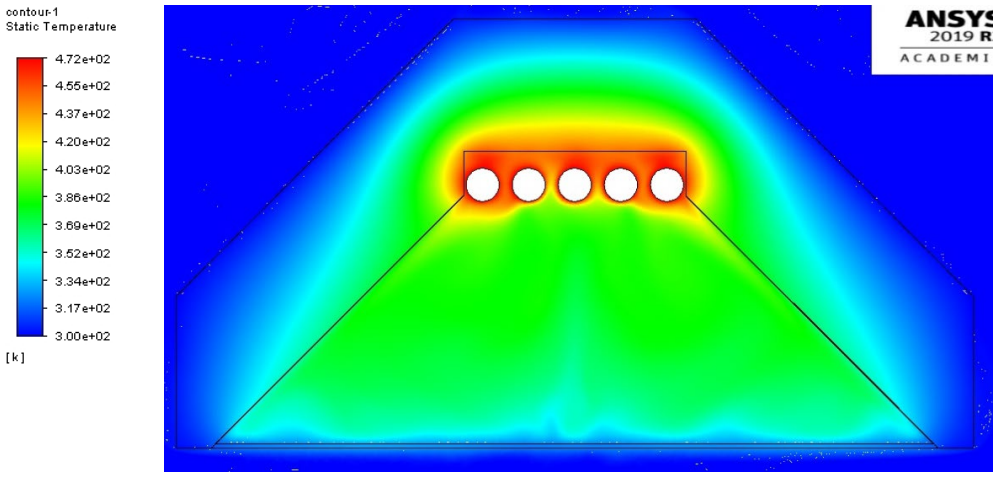

Figure 15 Temperature contours for validation test case II for a tube temperature of 198.5 °C

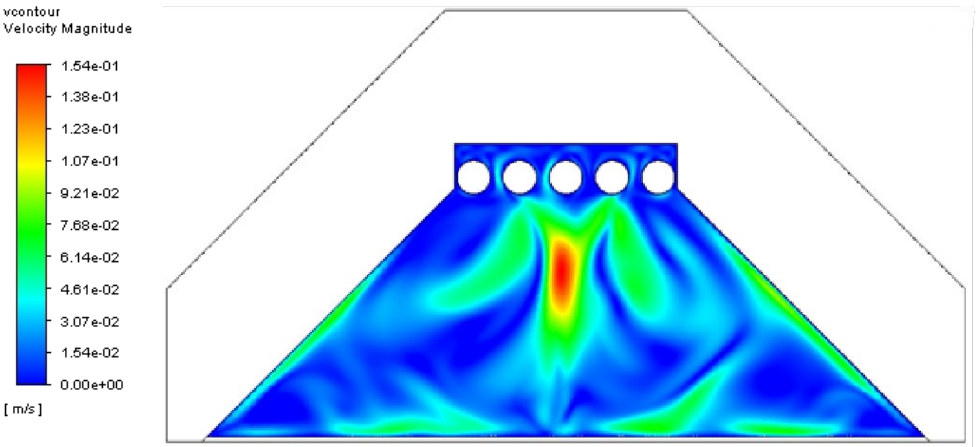

Figure 16 Velocity magnitude contours for validation test case II for a tube temperature of 198.5 °C

Figure 15 and Figure 16 show the temperature and velocity contours of the receiver. The temperature contours confirm that the highest temperature occurs around the backs of the tubes, where velocity magnitudes are limited, similar to results obtained by Moghimi et al. (2015). In addition, there is a high degree of thermal stratification of the air within the receiver cavity as expected (Manikumar et al., 2012; Manikumar and Valan Arasu, 2014). There are areas of more intense circulation near the inner surface of the glass and side walls, as well as at the centre of the cavity where the two circulation cells overlap. This is in line with results by Facão and Oliveira (2011) and Saxena et al. (2016). The slight asymmetry in the displayed solution is indicative of the slightly unstable behaviour of natural convection. This is also illustrated in the thermal plume shown in Figure 17. The small velocities propagating throughout the larger domain also indicate why the solution was sensitive to changes in the location of the pressure outlet boundaries for smaller domains. As the effects of the unsteadiness on the thermal solution are minimal, the simulation solver is kept as steady.

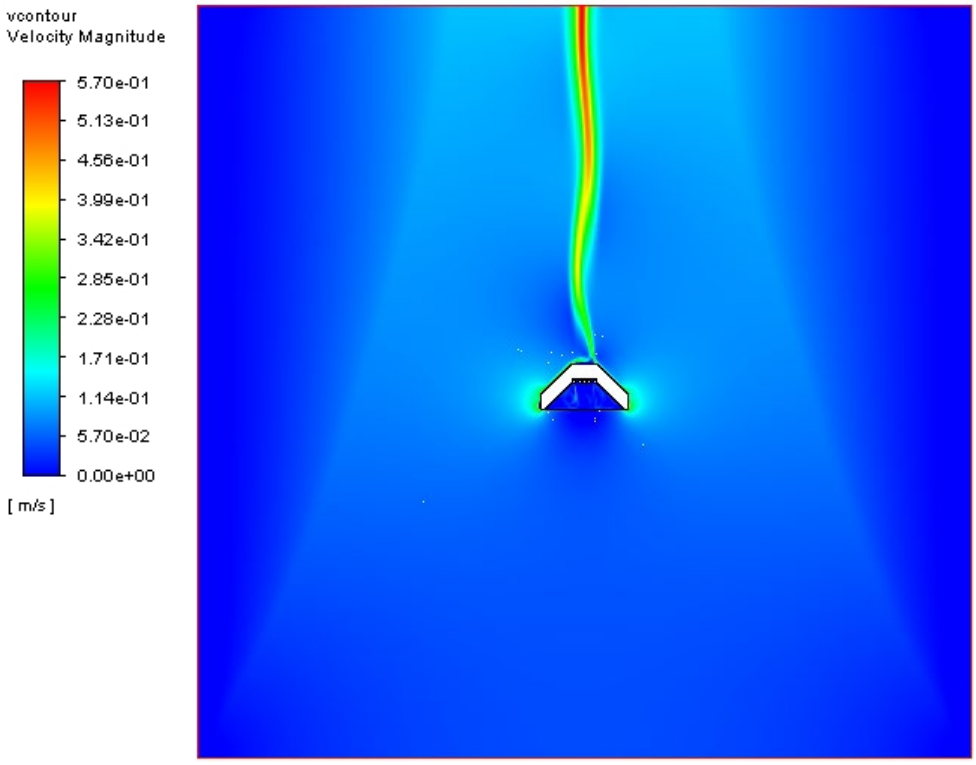

Figure 17 Velocity magnitude [m/s] contours for a tube temperature of 198.5 °C

The CFD results obtained from validation test case II are therefore considered to be in good agreement with the experimental results of Flores Larsen et al. (2012) and the expected thermal behaviour from other existing multitube receiver heat loss studies in the literature.

Based on the results from the two thermal validation cases, the proposed model settings and assumptions are considered valid for the 2D thermal studies used to consider the performance of the four candidate receivers.

6. Candidate receiver geometry

In order to determine the receiver geometry for each candidate receiver, a series of MCRT simulations were run using SolTrace (Wendelin et al., 2013) to generate response surfaces based on the peak optical performance of the field for a vertical sun (zero zenith and azimuth angles). The aperture width of the receiver (400 mm) and insulation thickness around the receiver (50 mm) are kept constant across all designs to maintain a basis of similarity for the thermal comparison. Traditionally, a CPC optic consists of involutes and macro focal ellipses (Chaves, 2016). In order to simplify the geometry within SolTrace, an adapted CPC type secondary was modelled using two parabolic segments with a focal point (f_x, f_y) using the following equation

$$(x - f_x)^2 = \frac{2}{C}(y - f_y) \quad (5)$$

The resultant optimum design consisted of parabolic segments with a gradient of $C = 5$ and a focal point at (0.03,0.03). Due to the asymmetric nature of the reflected radiation from the mirror field, this receiver was rotated by $\xi = 30°$. The geometry for the monotube receiver with adapted CPC type secondary is shown in Figure 18a. The typical design of a TERC-type monotube receiver is done on a point-by-point basis and consists of an involute mirror paired with a TERC-type secondary (Chaves et al., 2017).For this study, the involute section is also approximated as parabolic segments with a focal point at (0.03, -0.04) and a gradient of $C = 15$. The two TERC secondaries are approximated using linear sections, connected to the parabolic sections at angles τ_1 and τ_2, defined as follows:

$$\tau_1 = arctan\left(\frac{x_T}{H - y_T}\right) \quad (6)$$

$$\tau_2 = arctan\left(\frac{D - x_T}{H - y_T}\right) \quad (7)$$

The resultant optimum adapted TERC lengths are found to be 0.05m with the receiver rotated by the minimum angle of $\xi = 15°$, as shown in Figure 18b. The form of the receiver is relatively similar to the work of (Chaves et al., 2017) however the adapted TERC lengths are shorter.

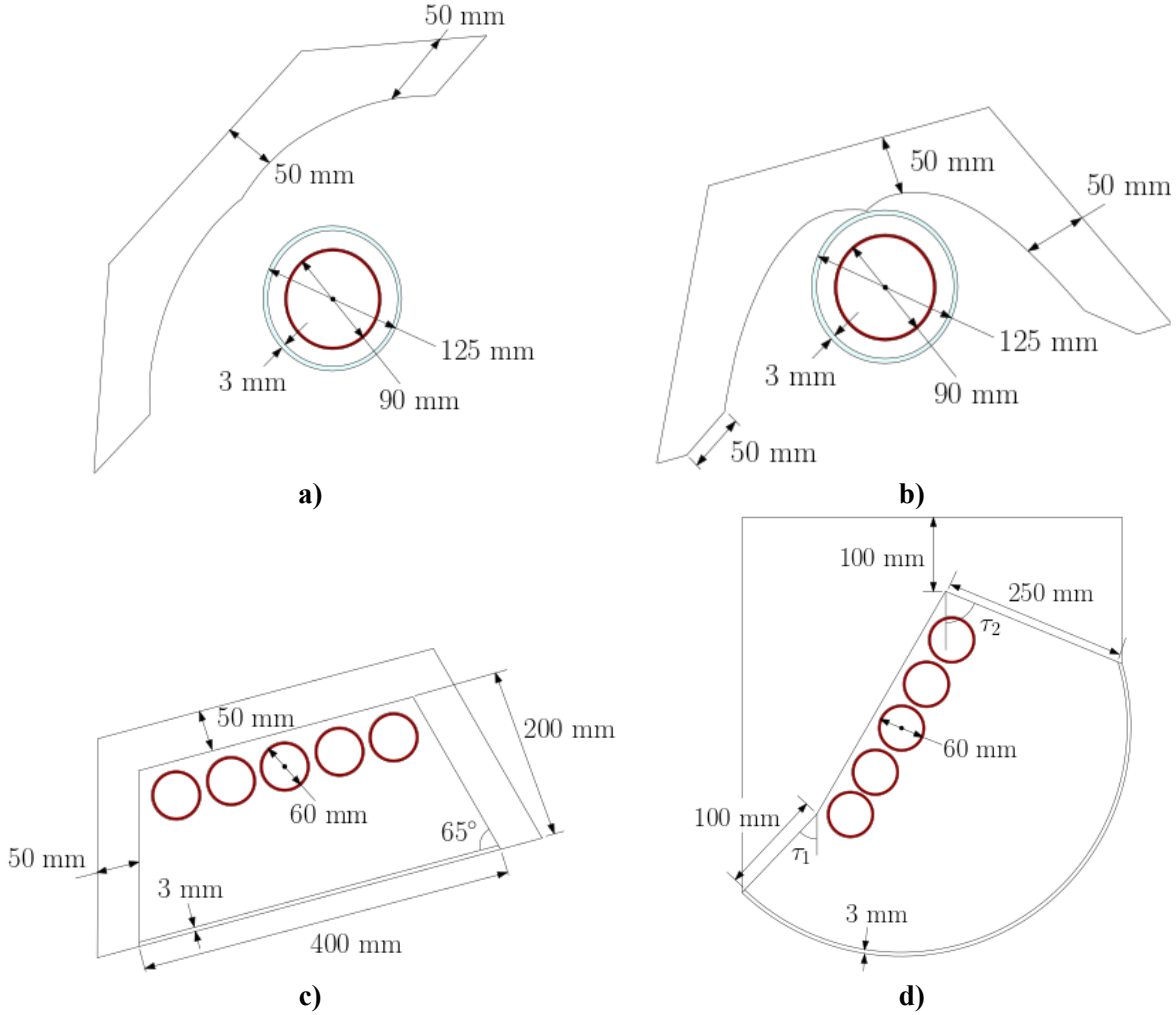

Figure 18 Receiver geometry for **a)** monotube receiver with adapted CPC type secondary, **b)** monotube receiver with adapted TERC type secondary, **c)** trapezoidal multitube receiver and **d)** multitube receiver with adapted TERC type secondary

For the trapezoidal multitube receiver, the area at the back of the receiver is calculated as a dependent parameter, using the aperture width (W_A), receiver depth (c), receiver interior angle (β), tube outer diameter (OD_{tube}) and the distance from the back of the tube to the back of the cavity (p_1).

$$b = W_A - \frac{2[c - (0.5OD_{tube} + p_1)]}{tan(\beta)} \quad (8)$$

The number of tubes (N_T) is then calculated as an integer value as follows

$$N_T = \frac{b}{OD_{tube} + p_2} \qquad N_T \in Z \quad (9)$$

In order to incorporate the conclusions from the literature regarding good thermal design, the gap between the tubes and the distance from the back of the receiver were chosen to be small (2 mm and 4 mm, respectively). The resultant receiver geometry is shown in Figure 18c, with a rotation angle of $\xi = 15°$. Lastly, the geometry for the multitube receiver with adapted TERC type secondary was determined using the equations (7) and (8) to determine the number of tubes and equations (5) and (6) to determine the angles τ_1 and τ_2. This larger angle requires an obtuse cover, as used by Horta et al. (2011) and Pye (2008). Due to the irregular nature of the geometry, the insulation shape is different from the designs used in the other receiver models and the receiver was rotated by an angle of $\xi = 60°$, as shown in Figure 18d.

7. Candidate receiver optical performance

The optical performance of the candidate receivers was determined through a series of SolTrace simulations. The emissive properties of the mirror field and receiver are listed in Table 5.

Table 5 Emissive properties of the mirror field and receiver

Material	Emissivity	Reference
Mirrors	Reflectance 1 – ε = 0.94	(Bellos et al., 2018c) (Kincaid et al., 2018) (Chaitanya Prasad et al., 2017) (Cagnoli et al., 2018)
Absorber tube(s)	Absorptance α = 0.95	(Cagnoli et al., 2018)
Borosilicate glass envelope for monotube receivers	Transmittance τ = 0.96	(Cagnoli et al., 2018)
Commercial glass cover for multitube receivers	Transmittance τ = 0.82	(Nicolau and Maluf, 2001)

In order to determine the appropriate number of rays to be used, a ray independence study was conducted for ray counts up to four million. Although there is no fixed limit to the number of rays that can be used in a simulation, the complexity of the geometry coupled with the available memory creates a practical limit (National Renewable Energy Laboratory, 2014). The error percentage is defined in terms of equation (10), with $\bar{P}_i$ the norm of the number of rays incident on the virtual aperture and P_i the number of rays for each simulation:

$$error = \frac{100\sqrt{(\bar{P}_i - P_i)^2}}{\bar{P}_i} \quad (10)$$

Figure 19 shows the resultant errors associated with the different numbers of rays. The error percentage was reduced to values lower than one percent for ray counts as low as 10 000. Given the complexity of the optics in this study, a relatively high ray count of one million was used for the subsequent optical performance studies in order to ensure an accurate radiation profile. This ray count is also in line with a number of optical performance studies (Bellos et al., 2018b; Hack et al., 2017; Tsekouras et al., 2018).

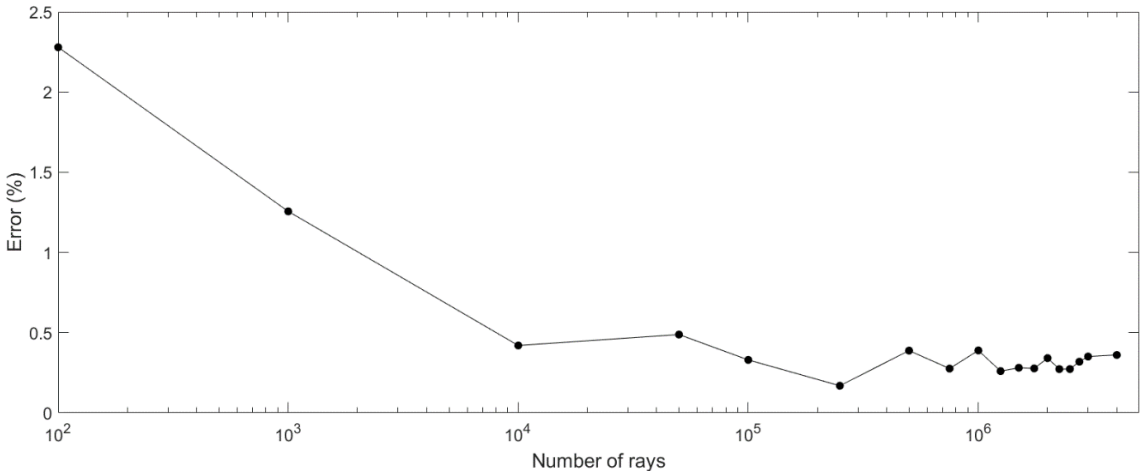

Figure 19 Ray sensitivity study for SolTrace simulations

The daily optical efficiency (η_{opt}) of these four receivers was determined by varying the zenith angle in 5° increments for a zero azimuth angle. This efficiency is calculated by dividing the sum of the absorbed radiation by the sum of the available energy for all the angle increments, according to equation (1). The resultant daily optical efficiencies of the chosen receivers paired with an etendue conserving compact linear Fresnel mirror field are listed in Table 6.

Table 6 Daily optical efficiency (η_{opt}) of different types of receivers paired with an etendue-conserving compact LFR field

Receiver type	Daily optical efficiency η_{opt} (%)
Adapted CPC-type monotube	51.29
Adapted TERC-type monotube	56.93
Standard trapezoidal multitube	53.69
Adapted TERC-type multitube	56.60

Note that had the same glass been used for both monotube and multitube receivers, the daily optical efficiency of the adapted TERC-type multitube receiver and standard trapezoidal multitube receiver would be 66.26% and 62.8% respectively. This increase in efficiency is due to the higher transmission associated with borosilicate glass relative to commercial glass. The use of commercial glass and simple geometry typically makes multitube receivers significantly cheaper than monotube receivers. Therefore, while the use of standard materials for each receiver does affect the optical and thermal performance, they are used within this study as it enables the realistic comparison between the receivers as they are found in industry and the incorporation of cost and structural comparisons in future work.

The best-performing receivers with these standard materials are the adapted TERC-type receivers, as their acceptance angles are designed based on the reflected radiation from the field. If the same glass is used the multitube receivers are the best performing, likely due to the larger total surface area of the absorber tube target. The worst-performing receiver is the adapted CPC-type monotube receiver, as the field imposes a large acceptance angle on the receiver. Using the optical design specified in equation (4), this requirement creates an open and shallow secondary shape with a large gap between the reflective surface and the absorber tube. This introduces higher optical losses (Rabl, 1985) and reduces the additional concentrating effect that can be obtained by the secondary. True CPC designs and methods to reduce optical losses for this type of secondary can be found in works by Chaves (2016), Winston (1978) and O'Gallagher *et al.* (1980). Similarly, true TERC designs can be found in the works by Chaves (2016) and Canavarro (2010).

8. Thermal studies of four receiver models

Domain and mesh sensitivity studies are run for each receiver model, with the resultant model domain and mesh specifications listed in Table 7.

Table 7 Domain and mesh specifications for the four receiver models

	Adapted CPC type monotube	Adapted TERC type monotube	TRAP multitube	Adapted TERC type multitube
Δx	0.05	5	4	7.5
x_{domain}	0.1	10	8	15
Δy	0.05	5	4	7.5
y_{domain}	0.1	10	8	15
Domain area [m^2]	0.01	100	64	225
Mesh cell count	775 444	851 204	377 302	777 146

The material properties used in these heat loss studies are listed in Table 9 in the Appendix. The insulating material used in all receivers is glass wool (with a thermal conductivity of k = 0.032 W/m-K at 293 K) and the surrounding domain is air with pressure outlets at the boundaries as with the test cases. The receiver inner walls have an emissivity of $\varepsilon = 0.1$, the absorber tubes have an absorptivity of $\alpha = 0.95$ and the outer walls have an emissivity of $\varepsilon = 0.75$ (Cagnoli et al., 2018; Reddy et al., 2018). The envelope used for the monotube receiver is made of borosilicate glass and vacuum conditions are used within the annulus. For the multitube receivers, a commercial glass cover is used with air inside the cavity.

The resultant heat loss per metre is listed in Table 8, with Figure 20 illustrating the heat loss over the specified temperature range for the four receiver models.

Table 8 Heat loss per metre versus absorber tube temperature for the four receiver models

Absorber tube temperature		**Heat loss per metre (W/m)**			
° C	**K**	**Adapted CPC type mono**	**Adapted TERC type mono**	**TRAP multi**	**Adapted TERC type multi**
50	323.15	28.90	24.46	51.77	69.39
100	373.15	117.73	101.50	193.06	249.58
150	423.15	250.13	215.99	401.59	544.04
200	473.15	436.35	375.00	676.56	881.38
250	523.15	687.79	592.06	1031.00	1373.63
300	573.15	1017.36	872.05	1497.05	1978.82
350	623.15	1439.26	1234.82	2084.26	2712.59
400	673.15	1969.40	1689.83	2823.28	3685.19
450	723.15	2627.30	2253.76	3723.38	4880.84

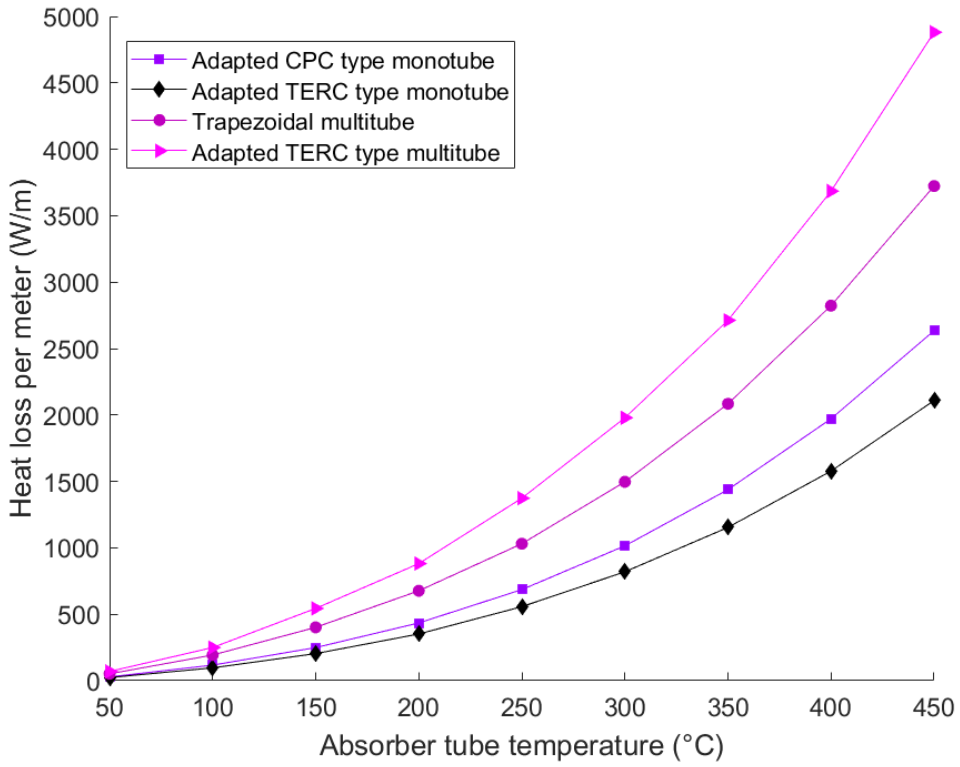

Figure 20 Heat loss per metre versus absorber tube temperature for the four receiver models

The exponential form of all four graphs demonstrates the dominance of radiation heat loss, especially at high temperatures. While all heat losses increase with the absorber tube temperature, the heat loss of the multitube models increased by a significantly higher degree. The trapezoidal receiver has higher heat losses than the adapted CPC- and TERC-type monotube receivers by a factor of 1.5 and 1.9, respectively, while the adapted TERC-type multitube has higher heat losses by factors of 2 and 2.5, respectively. This is partially due to the effect of the vacuum within the monotube receivers in limiting heat loss, and partially due to the multitube receivers having a higher absorber tube area. The adapted TERC-type multitube receiver has the highest heat loss of all the receiver models, with a higher heat loss than the trapezoidal multitube receiver by a factor of 1.32.

This is mainly caused by two factors. Firstly, as the majority of heat loss occurs through the glass cover, the larger glass area associated with the obtuse cavity increases the overall heat loss of the receiver. Secondly, the higher angle of rotation towards the mirror field causes more circulation within the receiver (Figure 21d), increasing internal convection loss. By contrast, the adapted TERC-type monotube receiver (Figure 21b) has the lowest heat loss of the receiver models. While both monotube receivers have low losses due to the evacuated annulus, the low angle of rotation and shape of the cavity within the adapted TERC-type receiver means that hot air is largely trapped within the cavity (Figure 21b), while within the adapted CPC-type receiver, a thermal plume rises freely (Figure 21a). This increases convection loss from the adapted CPC-type receiver and overall heat loss by a factor of 1.26. The trapezium (TRAP) multitube receiver (Figure 21c) experiences a thermal stratification similar to the second validation test case with the slightly slanted orientation due to the compact linear Fresnel mirror field, causing some external natural convection loss.

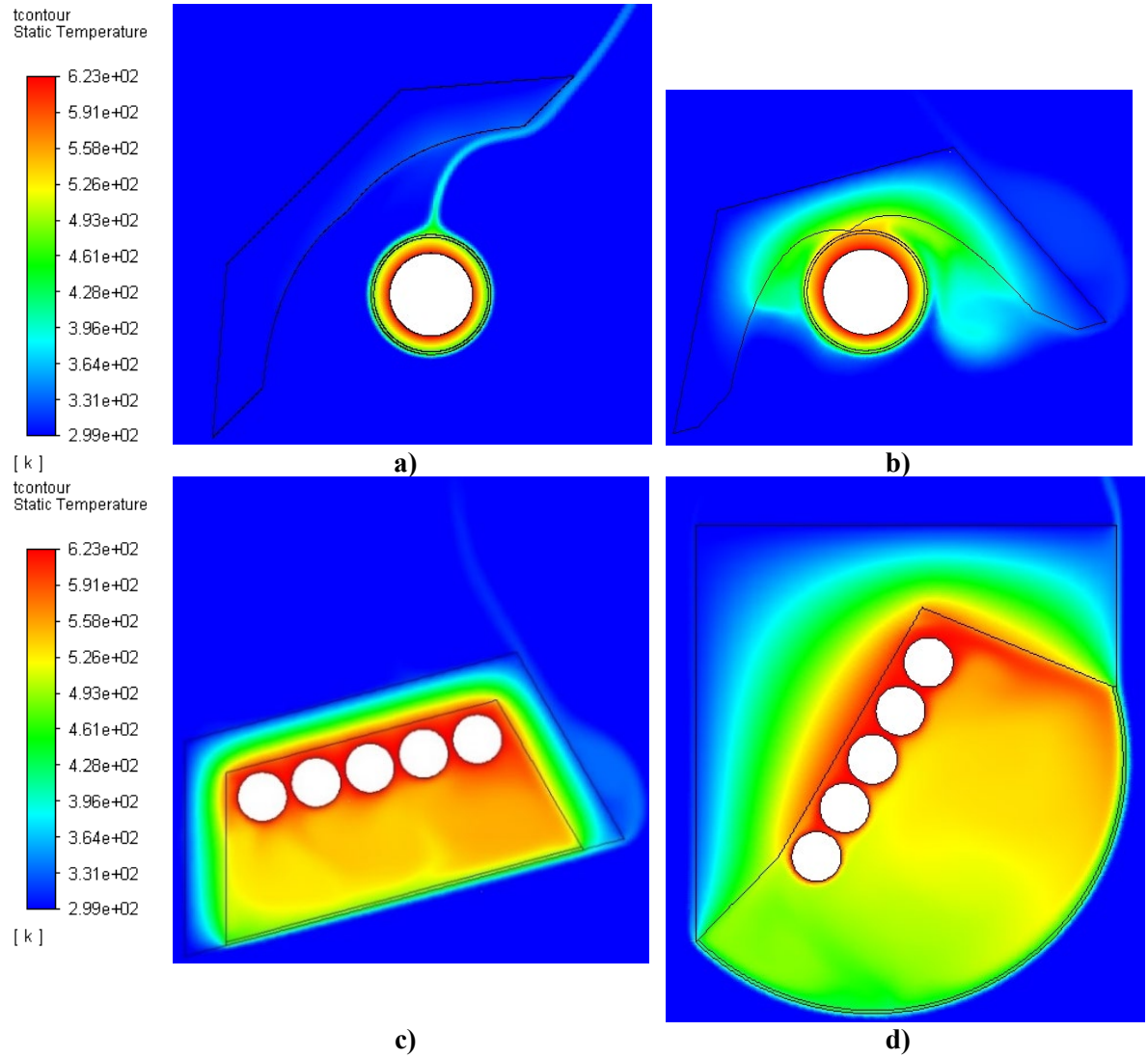

Figure 21 Temperature contours [K] for all four receiver models: a) adapted CPC type monotube; b) adapted TERC type monotube; c) TRAP multitube; and d) adapted TERC type multitube for a tube temperature of 623 K

The adapted TERC-type monotube is therefore the best performing on a thermal basis, followed by the adapted CPC-type monotube, the standard trapezoidal (TRAP) multitube and the adapted TERC-type multitube receivers, respectively. The thermal plume associated with this receiver is shown Figure 22. Very low velocities are present within the receiver cavity, further illustrating how hot air is trapped within the cavity. For all the receivers considered, the thermal plume would attach to any slanted sides of the geometry in the path of the plume.

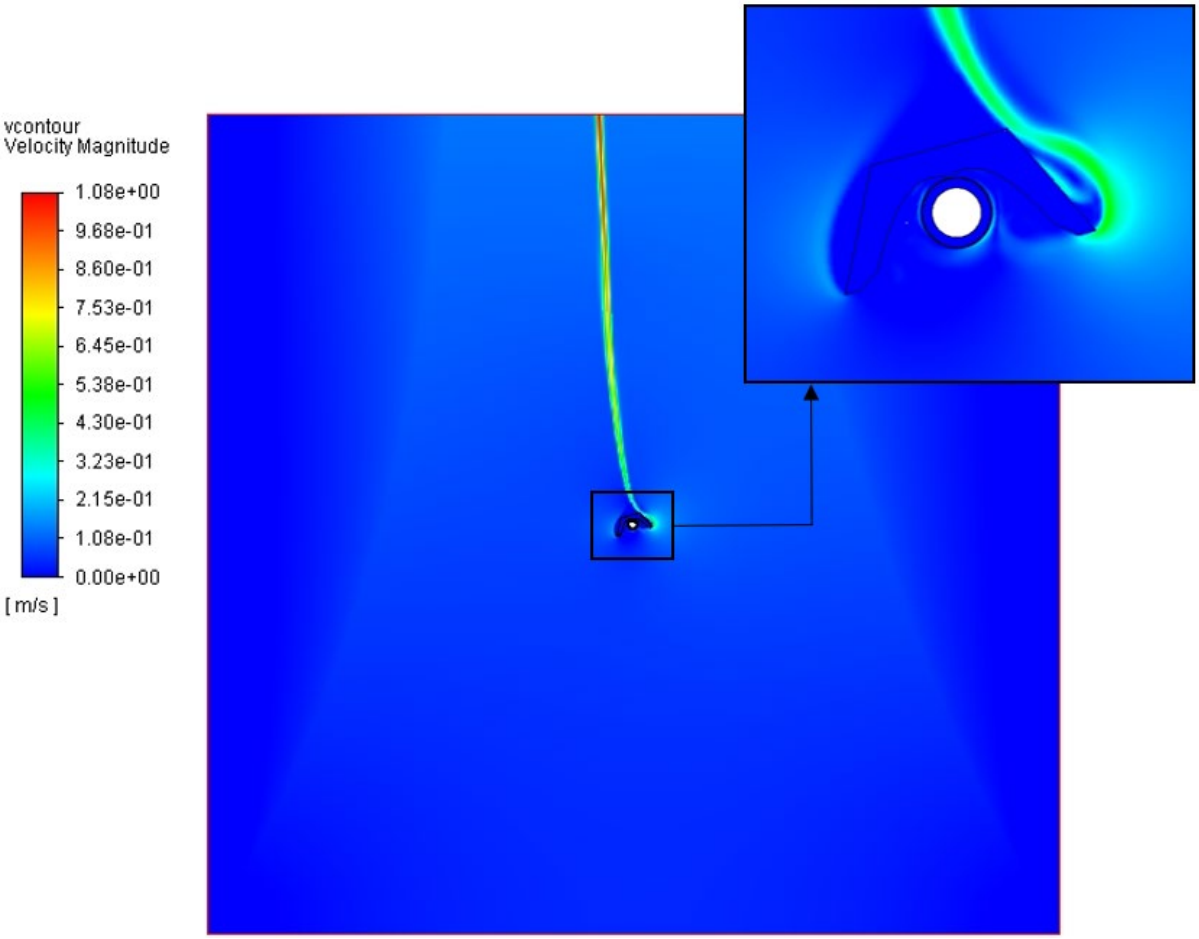

Figure 22 Velocity contour for an adapted TERC-type monotube receiver at a tube temperature of 623K

In addition to the conclusions drawn from the literature study regarding the reduction of thermal losses, two conclusions can be drawn from the thermal studies within this paper. Firstly, the lower the angle of rotation of the receiver geometry, the lower the thermal losses, due to the reduction in circulation within the cavity. Secondly, an obtuse receiver aperture increases the thermal losses of the receiver and based on this and the associated manufacturing complexity it would be preferable to approximate the required shape using straight segments.

9. Conclusion

The following was reported on in this paper

- The best conventional monotube receiver design from the literature was an evacuated monotube receiver with a CPC type secondary design. Other promising secondary designs were obtained through different optimisation strategies, but had a relatively similar form to the CPC type secondary.
- Limited research had been conducted on the best optical design for a conventional trapezoidal multitube receiver, but extensive research was found on the best thermal design. Therefore, the candidate design placed the absorber tubes close together at the back of the cavity. Where two designs performed similarly in an optical sense, the receiver with the smaller depth and aperture width was chosen.
- The candidate receivers were paired with an etendue-conserving compact linear Fresnel field, and through a series of optical optimisations, obtained daily optical efficiencies of $\eta_{opt} = 51.29\%$, $\eta_{opt} = 56.93\%$, $\eta_{opt} = 53.69\%$ and $\eta_{opt} = 56.60\%$ for the adapted CPC type monotube receiver,

the adapted TERC-type monotube receiver, the standard trapezoidal multitube receiver and the adapted TERC-type multitube receiver, respectively. It should be noted that the optical designs of the receivers were simplified; higher optical efficiencies would likely be achieved with true CPC and TERC-type secondaries.

- The thermal modelling settings and assumptions were validated against experimental work for an evacuated monotube receiver and a standard trapezoidal multitube receiver.
- Using 2D CFD simulations, the heat loss from the multitube receivers was determined to be greater than that from the monotube receivers by a factor of 1.5 to 2.5. The adapted CPC-type monotube receiver had higher heat losses than the adapted TERC-type monotube receiver by a factor of 1.26, while the adapted TERC-type multitube receiver had higher heat losses than the trapezoidal multitube receiver by a factor of 1.32.
- Based on the 2D CFD simulations, the angle of receiver rotation should be kept low in order to minimize circulation within the cavity. In addition, any obtuse aperture geometry should be approximated using straight segments.

In conclusion, while both adapted TERC-type receivers performed well optically, the adapted TERC-type multitube receiver had the highest thermal loss of all the receivers. In contrast, the adapted CPC-type monotube receiver performed comparatively poorly on an optical basis, but had very low thermal loss. Overall, the adapted TERC-type monotube receiver performed best on both an optical and a thermal basis, and is therefore determined to be the best receiver to pair with a state-of-the-art etendue-conserving compact linear Fresnel field.

However, it should be noted that the best receiver design will depend on the application; if the temperature of the heat transfer fluid is high, an evacuated monotube receiver would be preferable. However, if temperatures are relatively low and a reduction in costs is prioritised, a multitube receiver would be preferable. Given the decoupled nature of the study, the performance evaluation within this paper can be used as a tool to better inform those trade-offs.

Acknowledgements

The authors would like to acknowledge the support of the University of Pretoria (South Africa) and the South African Department of Science and Innovation for student bursary support.

References

Abbas, R., Muñoz, J., Martínez-Val, J.M., 2012. Steady-state thermal analysis of an innovative receiver for linear Fresnel reflectors. Appl. Energy 92, 503–515. https://doi.org/10.1016/j.apenergy.2011.11.070

ANSYS Inc, 2019a. Fluent 2019 R3 Theory Guide [WWW Document].

ANSYS Inc, 2019b. Fluent 2019 R3 User's Guide.

Bellos, E., Tzivanidis, C., Papadopoulos, A., 2018a. Optical and thermal analysis of a linear Fresnel reflector operating with thermal oil, molten salt and liquid sodium. Appl. Therm. Eng. 133, 70–80. https://doi.org/10.1016/j.applthermaleng.2018.01.038

Bellos, E., Tzivanidis, C., Papadopoulos, A., 2018b. Secondary concentrator optimization of a linear Fresnel reflector using Bezier polynomial parametrization. Sol. Energy 171, 716–727. https://doi.org/10.1016/j.solener.2018.07.025

Bellos, E., Tzivanidis, C., Papadopoulos, A., 2018c. Daily, monthly and yearly performance of a linear Fresnel reflector. Sol. Energy 173, 517–529. https://doi.org/10.1016/j.solener.2018.08.008

Bennett, H.E., Porteus, J.O., 1961. Relation between surface roughness and specular reflectance at

584 normal incidence. J. Opt. Soc. Am. 51, 123. https://doi.org/10.1364/josa.51.000123

585 Burkholder, F., Kutscher, C.F., 2009. Heat loss testing of Schott's 2008 PTR70 parabolic trough
586 receiver [WWW Document]. NREL Tech. Rep. URL
587 http://www.nrel.gov/docs/fy09osti/45633.pdf (accessed 6.12.20).

588 Cagnoli, M., Mazzei, D., Procopio, M., Russo, V., Savoldi, L., Zanino, R., 2018. Analysis of the
589 performance of linear Fresnel collectors: Encapsulated vs. evacuated tubes. Sol. Energy 164,
590 119–138. https://doi.org/10.1016/j.solener.2018.02.037

591 Canavarro, D., 2010. Modeling linear solar collectors of the Fresnel-type; application to an innovative
592 CLFR collector etendue-matched. MSc Thesis, Instituto Superior Técnico Lisbon, Portugal.

593 Canavarro, D., Chaves, J., Collares-Pereira, M., 2016. A novel compound elliptical-type concentrator
594 for parabolic primaries with tubular receiver. Sol. Energy 134, 383–391.
595 https://doi.org/10.1016/j.solener.2016.05.027

596 Canavarro, D., Chaves, J., Collares-Pereira, M., 2014. Simultaneous Multiple Surface method for
597 linear Fresnel concentrators with tubular receiver. Sol. Energy 110, 105–116.
598 https://doi.org/10.1016/j.solener.2014.09.002

599 Chaitanya Prasad, G.S., Reddy, K.S., Sundararajan, T., 2017. Optimization of solar linear Fresnel
600 reflector system with secondary concentrator for uniform flux distribution over absorber tube.
601 Sol. Energy 150, 1–12. https://doi.org/10.1016/j.solener.2017.04.026

602 Chang, C., Li, X., Zhang, Q.Q., 2013. Experimental and numerical study of the heat transfer
603 characteristics in solar thermal absorber tubes with circumferentially non-uniform heat flux, in:
604 Energy Procedia. Elsevier Ltd, pp. 305–313. https://doi.org/10.1016/j.egypro.2014.03.033

605 Chaves, J., 2016. Introduction to nonimaging optics, Second ed. ed. Taylor & Francis, New York,
606 United States.

607 Chaves, J., Collares-Pereira, M., 2010. Etendue-matched two-stage concentrators with multiple
608 receivers. Sol. Energy 84, 196–207. https://doi.org/10.1016/j.solener.2009.10.022

609 Chaves, J., Collares-Pereira, M., Canavarro, D., 2017. Compact linear Fresnel reflector solar
610 concentrator designed for direct molten salt operation as heat transfer fluid in evacuated tubes.
611 WO 2017/131544 A1. WO 2017/131544 Al.

612 Choudhury, C., Sehgal, H.K., 1986. A Fresnel strip reflector-concentrator for tubular solar-energy
613 collectors. Appl. Energy 23, 143–154. https://doi.org/10.1016/0306-2619(86)90036-X

614 Craig, K.J., Moghimi, M.A., Rungasamy, A.E., Marsberg, J., Meyer, J.P., 2016. Finite-volume ray
615 tracing using computational fluid dynamics in linear focus CSP applications. Appl. Energy 183,
616 241–256. https://doi.org/10.1016/j.apenergy.2016.08.154

617 Dabiri, S., Khodabandeh, E., Poorfar, A.K., Mashayekhi, R., Toghraie, D., Abadian Zade, S.A., 2018.
618 Parametric investigation of thermal characteristic in trapezoidal cavity receiver for a linear
619 Fresnel solar collector concentrator. Energy 153, 17–26.
620 https://doi.org/10.1016/j.energy.2018.04.025

621 Dey, C.J., 2004. Heat transfer aspects of an elevated linear absorber. Sol. Energy 76, 243–249.
622 https://doi.org/10.1016/j.solener.2003.08.030

623 DuPont Teigin Films, 2003. Mylar physical-thermal properties [WWW Document]. URL
624 http://usa.dupontteijinfilms.com/informationcenter/downloads/Physical_And_Thermal_Propertie
625 s.pdf (accessed 10.17.19).

626 Facão, J., Oliveira, A.C., 2011. Numerical simulation of a trapezoidal cavity receiver for a linear
627 Fresnel solar collector concentrator. Renew. Energy 36, 90–96.
628 https://doi.org/10.1016/j.renene.2010.06.003

629 Feuermann, D., Gordon, J.M., 1991. Analysis of a two-stage linear fresnel reflector solar
630 concentrator. J. Sol. Energy Eng. 113, 272–279. https://doi.org/10.1115/1.2929973

631 Flores Larsen, S., Altamirano, M., Hernández, A., 2012. Heat loss of a trapezoidal cavity absorber for
632 a linear Fresnel reflecting solar concentrator. Renew. Energy 39, 198–206.
633 https://doi.org/10.1016/j.renene.2011.08.003

634 Goswami, R.P., Negi, B.S., Sehgal, H.K., Sootha, G.D., 1990. Optical designs and concentration
635 characteristics of a linear Fresnel reflector solar concentrator with a triangular absorber. Sol.
636 Energy Mater. 21, 237–251. https://doi.org/10.1016/0741-983X(90)90023-U

637 Grena, R., Tarquini, P., 2011. Solar linear Fresnel collector using molten nitrates as heat transfer fluid.
638 Energy 36, 1048–1056. https://doi.org/10.1016/j.energy.2010.12.003

639 Guerreiro, L., Canavarro, D., Collares-Pereira, M., 2011. Increasing the cost effectiveness of CSP
640 technologies through the development of a new CLFR "etendue matched" collector, in: 30th
641 ISES Biennial Solar World Congress 2011, SWC 2011. pp. 3878–3886.
642 https://doi.org/10.18086/swc.2011.25.14

643 Guerreiro, L., Canavarro, D., Collares Pereira, M., 2015. Efficiency improvement and potential LCOE
644 reduction with an LFR-XX SMS plant with storage, in: Energy Procedia. Elsevier Ltd, pp. 868–
645 878. https://doi.org/10.1016/j.egypro.2015.03.112

646 Hack, M., Zhu, G., Wendelin, T., 2017. Evaluation and comparison of an adaptive method technique
647 for improved performance of linear Fresnel secondary designs. Appl. Energy 208, 1441–1451.
648 https://doi.org/10.1016/j.apenergy.2017.09.009

649 Heimsath, A., Cuevas, F., Hofer, A., Nitz, P., Platzer, W.J., 2014. Linear Fresnel collector receiver:
650 Heat loss and temperatures, in: Energy Procedia. Elsevier Ltd, pp. 386–397.
651 https://doi.org/10.1016/j.egypro.2014.03.042

652 Hofer, A., Cuevas, F., Heimsath, A., Nitz, P., Platzer, W.J., Scholl, S., 2015. Extended heat loss and
653 temperature analysis of three linear Fresnel receiver designs, in: Energy Procedia. Elsevier Ltd,
654 pp. 424–433. https://doi.org/10.1016/j.egypro.2015.03.049

655 Horta, P., Collares-pereira, M., Canavarro, D., Guerreiro, L.L., 2011. Modeling thermal losses in a
656 new CLFR etendue matched non-evacuated collector cavity, in: SolarPACES 2011, Grenada,
657 Spain. pp. 1–6.

658 Incropera, F.P., DeWitt, D.P., Bergman, T.L., Lavine, A.S., 2006. Fundamentals of heat and mass
659 transfer, Sixth ed. ed. John Wiley and Sons.

660 Jance, M.J., Morrison, G.L., Behnia, M., 2003. Natural convection and radiation within an enclosed
661 inverted absorber cavity, in: ANZSES From Fossils to Photons. Brisbane Australia, pp. 516–
662 527.

663 Jianfeng, L., Jing, D., Jianping, Y., 2010. Heat transfer performance of an external receiver pipe under
664 unilateral concentrated solar radiation. Sol. Energy 84, 1879–1887.
665 https://doi.org/10.1016/j.solener.2009.11.015

666 Kalogirou, S.A., 2014. Solar Energy Engineering: Processes and Systems, 2nd ed. ed, Solar Energy
667 Engineering. Elsevier. https://doi.org/10.1016/b978-0-12-397270-5.00010-8

668 Khan, K.., Khamrul, M.D., 1999. Copper oxide coating for use in a linear solar Fresnel reflecting
669 concentrating collector. Renew. Energy 7, 603–608.

670 Kincaid, N., Mungas, G., Kramer, N., Wagner, M., Zhu, G., 2018. An optical performance
671 comparison of three concentrating solar power collector designs in linear Fresnel, parabolic
672 trough, and central receiver. Appl. Energy 231, 1109–1121.
673 https://doi.org/10.1016/j.apenergy.2018.09.153

Lienhard, J.H., 2008. A Heat Transfer, Third ed. ed. Phlogiston Press, Cambridge, United States.

Loenen, E., Van Der Tempel, L., 1996. Determination of absorption coefficients of glasses at high temperatures, by measuring the thermal emission, Phillips Research.

Lovegrove, K., Stein, W., 2020. Concentrating Solar Power Technology Principles, Developments, and Applications, 2nd ed. ed. Woodhead Publishing.

Manikumar, R., Arasu, A.V., Jayaraj, S., 2012. Computational fluid dynamics analysis of a trapezoidal cavity absorber used for the linear Fresnel reflector solar concentrator system. J. Renew. Sustain. Energy 4, 0–18. https://doi.org/10.1063/1.4772636

Manikumar, R., Valan Arasu, A., 2014. Heat loss characteristics study of a trapezoidal cavity absorber with and without plate for a linear Fresnel reflector solar concentrator system. Renew. Energy 63, 98–108. https://doi.org/10.1016/j.renene.2013.09.005

Mathur, S. S., Kandpal, T.C., Negi, B.S., 1991. Optical design and concentration characteristics of linear Fresnel reflector solar concentrators- II. Mirror elements of equal width. Energy Convers. Manag. 31, 221–232.

Mathur, S.S., Kandpal, T.C., Negi, B.S., 1991. Optical design and concentration characteristics of linear Fresnel reflector solar concentrators - I. Mirror elements of varying width. Energy Convers. Manag. 31, 205–219.

Moghimi, M.A., 2017. Optical, thermal and economic optimisation of a linear Fresnel collector. Ph.D. Thesis University of Pretoria, South Africa.

Moghimi, M.A., Craig, K.J., Meyer, J.P., 2015. Optimization of a trapezoidal cavity absorber for the linear Fresnel reflector. Sol. Energy 119, 343–361. https://doi.org/10.1016/j.solener.2015.07.009

Moghimi, M.A., Craig, K.J.J., Meyer, J.P.P., 2017. Simulation-based optimisation of a linear Fresnel collector mirror field and receiver for optical, thermal and economic performance, Solar Energy. Elsevier Ltd. https://doi.org/10.1016/j.solener.2017.06.001

Moghimi, M.A.A., Rungasamy, A.E., Craig, K.J.J., Meyer, J.P.P., 2016. Introducing CFD in the optical simulation of linear Fresnel collectors, in: AIP Conference Proceedings. https://doi.org/10.1063/1.4949039

Montes, M.J., Abbas, R., Muñoz, M., Muñoz-Antón, J., Martínez-Val, J.M., 2017a. Advances in the linear Fresnel single-tube receivers: Hybrid loops with non-evacuated and evacuated receivers. Energy Convers. Manag. 149, 318–333. https://doi.org/10.1016/j.enconman.2017.07.031

Montes, M.J., Abbas, R., Rovira, A., Muñoz-Antón, J., Martínez-Val, J.M., 2017b. Methodology for the thermal characterization of linear Fresnel collectors: Comparative of different configurations and working fluids. AIP Conf. Proc. 1850. https://doi.org/10.1063/1.4984403

Natarajan, S.K., Reddy, K.S., Mallick, T.K., 2012. Heat loss characteristics of trapezoidal cavity receiver for solar linear concentrating system. Appl. Energy 93, 523–531. https://doi.org/10.1016/j.apenergy.2011.12.011

National Renewable Energy Laboratory, 2014. Concentrating Solar Power SolTrace FAQs [WWW Document]. URL https://www.nrel.gov/csp/soltrace-faqs.html (accessed 10.12.20).

Negi, B., Mathur, S., Kandpal, T., 1989. Optical and thermal performance of a linear Fresnel reflector solar concentrator. Sol. Wind Technol. 6, 589–593.

Nicolau, V.D.P., Maluf, F.P., 2001. Determination of radiative properties of commercial glass, in: PLEA 2001 - The 18th Conference on Passive and Low Energy Architecture. Brazil.

O'Gallagher, J.J., Rabl, A., Winston, R., McIntire, W., 1980. Absorption enhancement in solar collectors by multiple reflections. Sol. Energy 24, 323–326. https://doi.org/10.1016/0038-

092X(80)90490-9

Parikh, A., Martinek, J., Mungas, G., Kramer, N., Braun, R., Zhu, G., 2019. Investigation of temperature distribution on a new linear Fresnel receiver assembly under high solar flux. Int. J. Energy Res. 43, 4051–4061. https://doi.org/10.1002/er.4374

Pye, J.D., 2008. System modelling of the compact linear Fresnel reflector. University of New South Wales.

Pye, J.D., Morrison, G.L., Behnia, M., 2003. Transient Modelling of cavity receiver heat transfer for the compact linear Fresnel reflector. Manuf. Eng. 1–9.

Qiu, Y., He, Y.L., Cheng, Z.D., Wang, K., 2015. Study on optical and thermal performance of a linear Fresnel solar reflector using molten salt as HTF with MCRT and FVM methods. Appl. Energy 146, 162–173. https://doi.org/10.1016/j.apenergy.2015.01.135

Rabl, A., 1985. Active Solar Collectors and Their Applications, New York.

Reddy, K.S., Balaji, S., Sundararajan, T., 2018. Heat loss investigation of 125kWth solar LFR pilot plant with parabolic secondary evacuated receiver for performance improvement. Int. J. Therm. Sci. 125, 324–341. https://doi.org/10.1016/j.ijthermalsci.2017.11.006

Reddy, K.S., Kumar, K.R., 2014. Estimation of convective and radiative heat losses from an inverted trapezoidal cavity receiver of solar linear Fresnel reflector system. Int. J. Therm. Sci. 80, 48–57. https://doi.org/10.1016/j.ijthermalsci.2014.01.022

Reynolds, D.J., Jance, M.J., Behnia, M., Morrison, G.L., 2004. An experimental and computational study of the heat loss characteristics of a trapezoidal cavity absorber. Sol. Energy 76, 229–234. https://doi.org/10.1016/j.solener.2003.01.001

Rungasamy, A.E., 2020. Performance assessment and optimisation of different configurations of etendue-conserving compact linear Fresnel solar fields. Ph.D. Thesis, University of Pretoria, South Africa.

Rungasamy, A.E.E., Craig, K.J.J., Meyer, J.P.P., 2019. Comparative study of the optical and economic performance of etendue-conserving compact linear Fresnel reflector concepts. Sol. Energy 181, 95–107. https://doi.org/10.1016/j.solener.2019.01.081

Sahoo, S.S., Singh, S., Banerjee, R., 2013a. Steady state hydrothermal analysis of the absorber tubes used in linear Fresnel reflector solar thermal system. Sol. Energy 87, 84–95. https://doi.org/10.1016/j.solener.2012.10.002

Sahoo, S.S., Varghese, S.M., Suresh Kumar, C., Viswanathan, S.P., Singh, S., Banerjee, R., 2013b. Experimental investigation and computational validation of heat losses from the cavity receiver used in linear Fresnel reflector solar thermal system. Renew. Energy 55, 18–23. https://doi.org/10.1016/j.renene.2012.11.036

Saxena, A., Jhamaria, N., Singh, S., Sahoo, S.S., 2016. Numerical analysis of convective and radiative heat losses from trapezoidal cavity receiver in LFR systems. Sol. Energy 137, 308–316. https://doi.org/10.1016/j.solener.2016.08.026

Singh, P.L., Ganesan, S., Yàdav, G.C., 1999. Performance study of a linear Fresnel concentrating solar device (Technical Note). Renew. Energy 18, 409–416. https://doi.org/http://dx.doi.org/10.1016/S0960-1481(98)00805-2

Singh, P.L., Sarviya, R.M., Bhagoria, J.L., 2010a. Heat loss study of trapezoidal cavity absorbers for linear solar concentrating collector. Energy Convers. Manag. 51, 329–337.

Singh, P.L., Sarviya, R.M., Bhagoria, J.L., 2010b. Thermal performance of linear Fresnel reflecting solar concentrator with trapezoidal cavity absorbers. Appl. Energy 87, 541–550. https://doi.org/10.1016/j.apenergy.2009.08.019

Singh, R.N., Mathur, S.S., Kandpal, T.C., 1980. Some geometrical design aspects of a linear Fresnel. Energy Res. 4, 59–67.

Singhal, A.K., Singh, R.N., Kandpal, T.C., Mathur, S.S., 1982. Geometrical concentration characteristics of a linear Fresnel reflector using a fin receiver. Opt. Appl. XII.

Sootha, G.D., Negi, B.S., 1994. A comparative study of optical designs and solar flux concentrating characteristics of a linear fresnel reflector solar concentrator with tubular absorber. Sol. Energy Mater. Sol. Cells 32, 169–186. https://doi.org/10.1016/0927-0248(94)90302-6

Thermal Insulation Association of Southern Africa, 2013. TIASA Thermal insulation handbook, AAAMSA. South Africa.

Tsekouras, P., Tzivanidis, C., Antonopoulos, K., 2018. Optical and thermal investigation of a linear Fresnel collector with trapezoidal cavity receiver. Appl. Therm. Eng. 135, 379–388. https://doi.org/10.1016/j.applthermaleng.2018.02.082

Vouros, A., Mathioulakis, E., Papanicolaou, E., Belessiotis, V., 2019. On the optimal shape of secondary reflectors for linear Fresnel collectors. Renew. Energy 143, 1454–1464. https://doi.org/10.1016/j.renene.2019.05.044

Wendelin, T., Dobos, A.P., Lewandowski, A., 2013. SolTRACE: A new optical modeling tool for concentrating solar optics, National Renewable Energy Laboratory. https://doi.org/10.1115/ISEC2003-44090

White, F.M., 2011. Fluid mechanics, Seventh ed. ed. McGraw Hill.

Winston, R., 1978. Ideal flux concentrators with reflector gaps. Appl. Opt. 17, 1668. https://doi.org/10.1364/ao.17.001668

Zhu, G., 2017. New adaptive method to optimize the secondary reflector of linear Fresnel collectors. Sol. Energy 144, 117–126. https://doi.org/10.1016/j.solener.2017.01.005

Appendix: Material properties used within thermal CFD cases

Table 9 Material properties used within thermal CFD studies

	Density	**Thermal conductivity**	**Specific heat**	**Additional details**	**Reference**
	(kg/m^3)	**(W/m-K)**	**(J/kg-K)**		
Borosilicate glass	2 230	1.1	850	Refractive index I = 1.43 Absorption coefficient A = 33.5, $\lambda \leq 2.9$ µm A = 889.55, $\lambda > 2.9$ µm	(Loenen and Van der Tempel, 1996)
Commercial glass	2 650	1.5	786	Refractive index I = 1.4978 Absorption coefficient A = 37.128, $\lambda \leq 2.9$ µm A = 477.588, $\lambda > 2.9$ µm	(Nicolau and Maluf, 2001)

Mylar	1 390	0.5	1172.3	(DuPont Teigin Films, 2003)
Stainless steel 316	8 030	16.27	502.48	(ANSYS Inc, 2019b)
Carbon steel	7 818	54	670	(Incropera *et al.*, 2006)
Glass wool	48	Piecewise linear	446	(Thermal Insulation Association of Southern Africa, 2013)
Vacuum	1.205	10^{-4}	1	(Parikh *et al.*, 2019)
Air	Incompressible ideal gas	Piecewise linear	Piecewise linear	(Lienhard and Lienhard, 2003)